

This is the peer reviewed version of the following article:

Origin and age of zircon-bearing chromitite layers from the Finero phlogopite peridotite (Ivrea-Verbanò Zone, Western Alps) and geodynamic consequences / Alberto, Z., Giovanardi, T., Antonio, L., Massimo, T., Fu Yuan, W.u., Luigi, D., Mazzucchelli, M.. - In: LITHOS. - ISSN 0024-4937. - STAMPA. - 262:(2016), pp. 58-74. [10.1016/j.lithos.2016.06.015]

*Terms of use:*

The terms and conditions for the reuse of this version of the manuscript are specified in the publishing policy. For all terms of use and more information see the publisher's website.

19/06/2026 01:15

(Article begins on next page)

## Accepted Manuscript

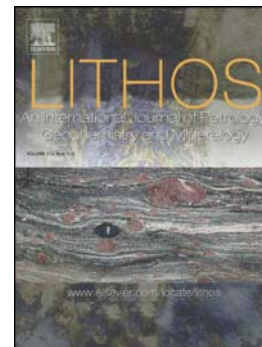
Origin and age of zircon-bearing chromitite layers from the Finero Phlogopite Peridotite (Ivrea-Verbano Zone, western Alps) and geodynamic consequences

Alberto Zanetti, Tommaso Giovanardi, Antonio Langone, Massimo Tiepolo, Fu-Yuan Wu, Luigi Dallai, Maurizio Mazzucchelli

PII: S0024-4937(16)30128-1  
DOI: doi: [10.1016/j.lithos.2016.06.015](https://doi.org/10.1016/j.lithos.2016.06.015)  
Reference: LITHOS 3961

To appear in: *LITHOS*

Received date: 3 December 2015  
Accepted date: 17 June 2016



Please cite this article as: Zanetti, Alberto, Giovanardi, Tommaso, Langone, Antonio, Tiepolo, Massimo, Wu, Fu-Yuan, Dallai, Luigi, Mazzucchelli, Maurizio, Origin and age of zircon-bearing chromitite layers from the Finero Phlogopite Peridotite (Ivrea-Verbano Zone, western Alps) and geodynamic consequences, *LITHOS* (2016), doi: [10.1016/j.lithos.2016.06.015](https://doi.org/10.1016/j.lithos.2016.06.015)

This is a PDF file of an unedited manuscript that has been accepted for publication. As a service to our customers we are providing this early version of the manuscript. The manuscript will undergo copyediting, typesetting, and review of the resulting proof before it is published in its final form. Please note that during the production process errors may be discovered which could affect the content, and all legal disclaimers that apply to the journal pertain.

1 **Origin and age of zircon-bearing chromitite layers from the Finero Phlogopite Peridotite**  
2 **(Ivrea-Verbano Zone, western Alps) and geodynamic consequences**

3 Alberto Zanetti<sup>1</sup>, Tommaso Giovanardi<sup>2</sup>, Antonio Langone<sup>1</sup>, Massimo Tiepolo<sup>3</sup>, Fu-Yuan Wu<sup>4</sup>,  
4 Luigi Dallai<sup>5</sup>, Maurizio Mazzucchelli<sup>6,1</sup>.

5  
6 1Istituto di Geoscienze e Georisorse - CNR, Unità di Pavia, Via Ferrata, 1, I-27100 Pavia, Italy;

7 2Istituto de Geociências, Universidade de São Paulo, Rua do Lago, 562, Cidade Universitária,  
8 05508-900 São Paulo, Brazil;

9 3Dipartimento di Scienze della Terra 'Ardito Desio', Università degli Studi di Milano, Via  
10 Mangiagalli/Botticelli, 32/23, I-20133 Milano, Italy;

11 4State Key Laboratory of Lithospheric Evolution, Institute of Geology and Geophysics, Chinese  
12 Academy of Sciences, P. O. Box 9825, 100029 Beijing, China;

13 5Istituto di Geoscienze e Georisorse - CNR, Sede di Pisa, Via Giuseppe Moruzzi, 1, I-56124 Pisa,  
14 Italy;

15 6Dipartimento di Scienze Chimiche e Geologiche, Università di Modena e Reggio Emilia, Via  
16 Campi, 103, I-41125 Modena, Italy.

17

18 Corresponding Author: Tommaso Giovanardi; e-mail: [tommaso.giovanardi@gmail.com](mailto:tommaso.giovanardi@gmail.com)

19

20 **Abstract**

21 An investigation has been performed on three chromitite layers segregated in dunite bodies of the  
22 Phlogopite Peridotite mantle unit in the Finero Complex (FPP, Ivrea–Verbano Zone, Southern  
23 Alps) aimed at providing new constraints to their origin and evolution.

24 Field relationships, the sub-chondritic Hf isotopic composition of the zircons ( $\epsilon\text{Hf}_{(188)}$  as low as -  
25 5.4), the heavy O isotopic composition of zircons and pyroxenes ( $\delta^{18}\text{O}$  up to 6.9‰), the strict  
26 similarity of the trace element composition between the clinopyroxenes and amphiboles from the

27 chromitites and those from the phlogopite harzburgites and pyroxenites forming the typical FPP  
28 association, as well as the REE composition of zircons, which approaches equilibrium with the  
29 associate clinopyroxene, suggest that the studied chromitites were segregated from melts, highly  
30 contaminated from continental crust, during the pervasive cycle of metasomatism recorded by the  
31 FPP. A LA-ICP-HRMS survey of chromitite zircon grains has provided Early Jurassic U-Pb ages  
32 mostly between  $199 \pm 3$  Ma and  $178 \pm 2$  Ma, with a pronounced peak at 187 Ma. Relevant  
33 exceptions are inherited domains of two grains giving Triassic ages of  $242 \pm 7$  Ma and  $229 \pm 7$  Ma,  
34 and a third homogeneous zircon giving  $208 \pm 3$  Ma. Our geochronological data and those reported  
35 in the literature show that the FPP chromitites have zircon populations with different internal CL  
36 textures, but the same sub-chondritic Hf isotopic composition, which define an overall U-Pb age  
37 span from ~290 Ma to 180. The segregation of the chromitite layers and the main pervasive  
38 metasomatism likely occurred in the Early Permian (in a post-collisional, transtensional setting) or  
39 before (possibly, in a subduction-related setting). The rejuvenation of the zircon ages was  
40 accompanied by a progressive disappearance of the internal zoning, interpreted as the result of a  
41 prolonged residence at mantle depths with progressive re-equilibration of the U-Pb system due to  
42 thermal perturbations. The age peak at ~187 Ma is argued to constrain the timing of FPP  
43 exhumation at shallower, crustal levels. This process was characterised by an important reheating  
44 event, possibly due to lithospheric hyperextension. The evolution of the FPP appears completely  
45 different than that of mantle bodies of the central IVZ (i.e. the Val Sesia-Type bodies), which were  
46 emplaced within the continental crust, as part of accretionary prisms, at or before the end of the  
47 Variscan orogeny.

48

49 **Keywords:** Finero; zircon; mantle; chromitite; metasomatism.

50

51 **Introduction**

52 The Ivrea-Verbano Zone (IVZ, Southern Alps, Italy-Switzerland) consists of a worldwide famous  
53 section of lower continental crust. The reference geodynamic model developed after detailed field,  
54 geochronological and geochemical investigation of its central part (i.e. Sesia and Sessera Valleys)  
55 involves Early Permian under- and intra-plating of mafic melts, which interacted with granulite to  
56 amphibolite-facies metamorphic basement and evolved towards acid compositions producing  
57 granite intrusions and rhyolite volcanism (Quick et al., 1995, 2009; Sinigoi et al., 1996, 2011;  
58 Mazzucchelli et al., 2014).

59 Zanetti et al. (2013, 2014) pointed out that the northern sector of the IVZ records a number of  
60 structural, petrochemical and age anomalies with respect to such a model. For instance, there is now  
61 abundant evidence of the occurrence in the Finero Mafic Complex (northernmost IVZ) of  
62 widespread events of Triassic magmatism (Gebauer, 1993; Lu et al., 1997a,b; Hingerl et al., 2008;  
63 Zanetti et al., 2013, 2014; Klötzli, Personal Communication), with late alkaline veins and pockets  
64 (e.g. zircon-bearing diorites and nepheline diorite pegmatites) mostly showing Late Triassic to  
65 Early Jurassic ages (Oppizzi and Schaltegger, 1999; Grieco et al., 2001; Klötzli et al., 2007, 2009;  
66 Schaltegger et al., 2015, and references therein). Late Triassic intrusions of zircon-bearing diorites,  
67 associated to hornblendites (Stähle et al., 1990, 2001; Grieco et al., 2001), are also recorded by the  
68 associate mantle unit, the Finero Phlogopite Peridotite (FPP), which also shows peculiar late,  
69 discordant swarms of apatite-calcite-bearing gabbroic veins characterised by the presence of  
70 magmatic sapphirine (Giovanardi et al., 2013). A 225 Ma age has been found in a recrystallised rim  
71 of a zircon from a metasedimentary septum included in the intrusive External Gabbro unit and in a  
72 monazite from the adjacent Kinzigite Formation (Langone and Tiepolo, 2015).

73 These observations suggest the occurrence of two kinds of IVZ, the “Val Sesia”-Type (central IVZ)  
74 and the “Finero”-Type (northern IVZ), assumed to have had different tectono-magmatic evolutions  
75 (Rivalenti and Mazzucchelli, 2000; Zanetti et al., 2013, 2014; Mazzucchelli et al., 2014). Further  
76 main differences are the petrochemical features of the mantle bodies. The Val Sesia-Type mantle  
77 bodies are constituted by refractory spinel peridotites, virtually free from metasomatism away from

78 pyroxenites and dunite channels (Rivalenti et al., 1981, 1995; Mazzucchelli et al., 2009).  
79 Conversely, the Finero-Type mantle bodies are enriched in phlogopite and amphibole due to diffuse  
80 modal metasomatism (Rivalenti and Mazzucchelli, 2000; Zanetti et al., 2013; Mazzucchelli et al.,  
81 2014). According to the distribution of the different kinds of mantle peridotites, Zanetti et al. (2013)  
82 have speculatively proposed that their boundary may corresponds to the Anzola-Val Grande high  
83 temperature shear zone (HTSM in Fig. 1).

84 The FPP is the biggest mantle body of the northern IVZ. It shows a virtually complete  
85 recrystallization due to pervasive to channelled melt migrations (Zanetti et al., 1999). The pervasive  
86 metasomatism formed a main lithologic association constituted by phlogopite harzburgites  
87 associated to phlogopite pyroxenites (mainly websterites and orthopyroxenites), which do not show  
88 significant chemical gradients among them (Zanetti et al., 1999). The channelled migration stages  
89 formed dunite bodies, often containing stratiform to podiform chromites and, more rarely,  
90 pyroxenite and hornblendite layers (Cumming et al., 1987; Hartmann and Wedepohl, 1993; Zanetti  
91 et al., 1999; Seitz and Woodland, 2000; Grieco et al., 2001, 2004; Zaccarini et al., 2004; Raffone et  
92 al., 2006; Selverstone and Sharp, 2011; Giovanardi, 2012; Mazzucchelli et al., 2014). Relatively  
93 late melt migration events also formed peridotite and pyroxenite veins and bands (Zanetti et al.,  
94 1999, Grieco et al., 2001; Morishita et al., 2003, 2008; Matsumoto et al. 2005; Raffone et al., 2006).  
95 These are often characterised by the presence of apatite and carbonates, and usually exhibit marked  
96 modal and chemical gradients with respect to the host phlogopite harzburgite. Examples of these  
97 lithologies are the apatite-dolomite-bearing wehrlites (Zanetti et al., 1999; Raffone et al., 2006), as  
98 well as the apatite-bearing orthopyroxenites described by Morishita et al. (2003, 2008), and  
99 Matsumoto et al. (2005), these latter displaying Triassic ages.

100 Thanks to such a unique lithological association, the FPP is one of the most studied mantle  
101 sequence in the world (Fig. 1). Several papers have dealt with the age of the petrochemical  
102 processes and the geochemical affinity of the melts that migrated through it. These melts only  
103 marginally match the magmatic record of the associated crustal rocks of the Finero Mafic Complex

104 (Giovanardi et al., 2014). Despite this, the geodynamic evolution of the FPP is still controversial  
105 and the geochemical affinity of the metasomatic melts strongly debated. In particular,  
106 geochronological surveys reported in the literature give a very large age interval, spanning from the  
107 Early Permian to the Early Jurassic, which is difficult to reconcile with the evidence that the mantle  
108 bodies of the central IVZ (i.e. the Balmuccia body) were emplaced within the continental crust, as  
109 part of accretionary prisms, at or before the end of the Variscan orogeny.

110 A special opportunity to place geochronological constraints on the evolution of the FPP is  
111 represented by the occurrence of large amounts of primary zircon in the chromitites (Ferrario and  
112 Garuti, 1990; Grieco et al., 2001; Zaccarini et al., 2004). Thus, three chromitite swarms segregated  
113 in dunite bodies of the FPP were investigated. Zircon and associate minerals have been subjected to  
114 a detailed petrochemical investigation in order to shed light on i) the geochemical affinity of their  
115 parent melts, ii) the age of the metasomatism and iii) the geodynamic evolution of the mantle  
116 sequences in the Finero-Type IVZ.

117

### 118 **Geological setting and selected samples**

119 The IVZ represents the westernmost sector of the Southern Alps, which form the inner part of the  
120 Alpine orogen. The Southern Alps escaped Alpine subduction, thus preserving their lithospheric  
121 mantle roots. In the IVZ, the lithologies were tilted about of 90° at the end of the Middle Miocene  
122 (Wolff et al., 2012), as a consequence of a series of rotations started with the opening of the Jurassic  
123 Tethys and culminated with the Alpine collision and relaxation of the Alpine orogen (Rutter et al.,  
124 2007; Wolff et al., 2012; Beltrando et al., 2015). The Finero Complex outcrops as an antiform in the  
125 northernmost part of IVZ. The antiform core is composed by the Finero Phlogopite Peridotite  
126 mantle unit (FPP; Cawthorn, 1975), which is wrapped by an intercalation of mafic-ultramafic  
127 lithologies interpreted as pristine intrusive bodies (Cawthorn, 1975; Coltorti and Siena, 1984; Lu et  
128 al., 1997a, b), and referred to as the Finero Mafic Complex (Fig. 1). The latter consists (from the  
129 contact with the FPP outwards) of: i) the Layered Internal Zone (LIZ), ii) the Amphibole Peridotite

130 (AP) and iii) the External Gabbro (EG). To the N-NW, the Finero Complex is in contact across the  
131 Insubric line with an accretionary prism of the Alpine orogeny, namely the Sesia-Lanzo Zone,  
132 belonging to the Austroalpine domain (Fig. 1). To the S-SE, it is instead bounded by the metapelites  
133 and metavolcanics, from granulite-to-amphibolite-facies, of the Kinzigite Formation, i.e. the  
134 polymetamorphic basement of the Adria plate (Fig. 1).

135 In the FPP, stratiform to podiform chromitites mainly occur in dunite bodies. The petrogenesis of  
136 the FPP chromitites has previously been discussed by Ferrario and Garuti (1990), Garuti et al.  
137 (1997), Grieco et al. (2001, 2004) and Zaccarini et al. (2004), with the peculiar presence of zircons  
138 being firstly recognised by Ferrario and Garuti (1990). The chromitites locally contain abundant Fe-  
139 Ni-Cu-sulphides and Platinum Group Elements (PGE) minerals, but also zirconolite, baddeleyite,  
140 thorianite, uraninite, thorite or huttonite (Grieco et al., 2004; Zaccarini et al., 2004).

141 The dunite bodies were produced by stages of channelled melt migration (Grieco et al., 2001, 2004;  
142 Zaccarini et al., 2004). Most of them are elongated parallel to the mantle foliation and show sharp  
143 contacts with the host phlogopite-harzburgite and pyroxenite association. The abrupt change of the  
144 mineralogy is apparently the result of tectonic reactivation of the lithologic discontinuity. However,  
145 some gradational transitions between dunites and host harzburgites are preserved (Zaccarini et al.,  
146 2004). In particular, a gradational transition has been observed for peculiar dunite bodies having  
147 elongations highly discordant to the mantle foliation (Giovanardi, 2012).

148 Field observations indicate that large concordant dunites (up to 20 m across) i) may be virtually free  
149 from late magmatic segregations or layers; ii) contain chromitite layers (from a few mm to dm); iii)  
150 possess chromitites layers associate to the late intrusion of magmatic sheets, (Giovanardi, 2012).

151 Field relationships indicate that the chromitite segregation preceded formation of the other  
152 magmatic layers inside the dunite bodies, consistent with the observation reported by Grieco et al.  
153 (2001, 2004).

154 The chromitite swarms here studied formed in dunite bodies outcropping in different sectors of the  
155 FPP unit. At outcrop scale, no late phlogopite-amphibole-bearing magmatic layers are associated to

156 these chromitites. The samples selected are representative of two different chromitite end-members  
157 (Fig. 2). In particular, one sample (MR01CR) records only a large segregation of chromite with  
158 modest recovery of the previous texture dominated by deformed dunite olivine (hereafter Ol-  
159 chromitite; where Ol means olivine, Fig. 2c), while two samples document the complete recovery of  
160 the dunite texture, which is totally replaced by secondary chromite and orthopyroxene (hereafter  
161 Opx-chromitite, where Opx means orthopyroxene). The Ol-chromitite swarm, consisting of 1-cm  
162 thick parallel layers, outcrops in the area of Mount Sasso Rosso (MR01CR; Fig. 1). The chromitite  
163 layers are made of large, anhedral, locally round chromite grains crystallised in a strongly-deformed  
164 porphyroclastic dunite characterised by the presence of olivine porphyroclasts embedded in a fine-  
165 grained matrix. The latter basically consists of olivine, with subordinate, anhedral orthopyroxene, in  
166 part clearly overgrowing olivine. Very small clinopyroxene and amphibole grains have been  
167 detected by SEM-EDS inspection, while phlogopite is missing. Thorite was recognized during  
168 SEM-EDS inspection (Supplementary Material C). The two Opx-chromitites (FI09C04 and  
169 FI09C34; Fig. 2a, b) outcrop along the Cannobino river to the south of Finero, close to the bridge  
170 towards Provola (Fig. 1). The single chromitite layers of the Cannobino occurrences, up to 6 cm in  
171 thickness, locally merge in pockets up to 20 cm large (Fig. 2b). These chromitites show  
172 allotriomorphic texture and are mainly composed by chromite and orthopyroxene (chromite 75-55%  
173 by Vol.; orthopyroxene 35-15% by Vol.; Fig. 2d, e), with subordinate clinopyroxene, apparently in  
174 textural equilibrium with the other minerals. In these samples, olivine rarely occurs as very small,  
175 round relicts embedded in large orthopyroxenes. Phlogopite is missing, whereas rare amphibole  
176 grains, few tens of  $\mu\text{m}$  large, have been detected by SEM-EDS inspection. An Opx-chromitite  
177 sample with similar modal composition to those here studied was documented by Grieco et al.  
178 (2004).  
179 According to Ferrario and Garuti (1990), Grieco et al. (2001) and Zaccarini et al. (2004), zircons are  
180 up to 600  $\mu\text{m}$  long. Euhedral zircons occur within chromite and sometimes in olivine. Most

181 frequently, they are anhedral to subhedral, in interstitial position between chromite and olivine  
182 and/or orthopyroxene. Up to 25 zircons were observed in 50 mm<sup>2</sup> by Zaccarini et al. (2004).

183

#### 184 **Analytical methods**

185 Separation of orthopyroxene, clinopyroxene and zircon was performed with magnetic and  
186 chromatographic methods at the IGG-CNR, Pisa. The rocks were first grinded in two different  
187 granulometries: 0.250 to 0.125 mm and less than 0.125 mm. Minerals were then concentrated and  
188 purified by hand picking under a binocular microscope. Sixty-one zircons were separated from  
189 MR01CR, 11 from FI09C34 and 54 from FI09C04 and mounted in resin. Zircon internal structure  
190 was characterized with cathode-luminescence (CL) imaging by means of a SEM (Jeol JXA 840A  
191 model) at IGG-CNR, Pavia. Geochronological data were obtained with ELA-ICP-HRMS at the  
192 IGG-CNR, Pavia. The instrument couples an ArF excimer laser microprobe of 193 nm  
193 (Geolas200Q-Microlas) with a ThermoFinnigan Element I ICP-HRMS. Mass signals 202 (Hg), 204  
194 (Pb + Hg), 206 (Pb), 207 (Pb), 208 (Pb), 232 (Th) and 238 (U) were acquired in magnetic scan  
195 mode (Tiepolo, 2003). The laser was operated at a repetition rate of 5 Hz with a pulse-energy of  
196 about 12 J/cm<sup>2</sup>; Instrumental and laser-induced U/Pb fractionations were simultaneously corrected  
197 using as external standard the 1065 Ma 91500 reference zircon (Wiedenbeck et al., 1995). The same  
198 integration intervals and spot size were used on both the external standard and unknowns. During  
199 each analytical run reference zircon 02123 (295 Ma; Ketchum et al., 2001) was analysed together  
200 with unknowns for quality control, accuracy resulted better than 99%. The spot size was set to 20  
201 mm and laser fluency to 12J/cm<sup>2</sup>. Data reduction was carried out using the “Glitter” software  
202 package (van Achterbergh et al., 2001) setting at 1% the error of the external standard. During each  
203 analytical run the reproducibility on the standards was propagated to all determinations according to  
204 the equation in Horstwood et al. (2003). After this operation, analyses are considered accurate  
205 within quoted errors. . All the analyses in the present work yield count rates for <sup>204</sup>Pb at background  
206 level therefore no common Pb correction was carried out. The reader would however consider that

207 the relatively high background of Hg hampers the detection of low signals for  $^{204}\text{Pb}$ . Ages were  
208 calculated for  $^{207}\text{Pb}/^{206}\text{Pb}$ ,  $^{206}\text{Pb}/^{238}\text{U}$  and  $^{207}\text{Pb}/^{235}\text{U}$  ratios with  $2\sigma$  error (Tab. 1) using Isoplot  
209 software (Ludwig, 2003). Concordia ages were determined and concordia plots were constructed  
210 using the same software. All errors in the text are given at 2s level.

211 Mineral major element analyses were conducted with the electron microprobe JEOL 8200 Super  
212 Probe housed at the University of Milano (data are reported in Supplementary Material Tab. A) on  
213 petrographic sections after carbon coating. Analytical conditions were 15 kV of acceleration  
214 voltage, 15 nA of primary current beam, 10 s counting time for each element and 5 s counting time  
215 for the background.

216 Trace element concentrations in minerals have been determined with a LA-ICP-MS housed at IGG-  
217 C.N.R., Pavia (Supplementary Material Tab. B) consisting of a PerkinElmer SCIEX ELAN DCR-e  
218 quadrupole ICP-MS coupled with a Q-switched Nd:YAG laser source, model Brilliant (Quintel),  
219 whose fundamental emission (1064 nm) is converted to 266 nm by two harmonic generators. Spot  
220 diameter was typically 50-60  $\mu\text{m}$ . Data reduction was done with the GLITTER software, using the  
221 reference synthetic glass NISTSRM 610 as external standard. Si was used as internal standards for  
222 zircons, Ca for clinopyroxene. Precision and accuracy were assessed via repeated analysis of BCR-  
223 2g reference material, resulting better than  $\pm 10\%$  at ppm concentration level. More analytical  
224 details are reported in Miller et al. (2012).

225 *In-situ* Hf isotopic compositions of zircon have been determined at the State Key Laboratory of  
226 Lithospheric Evolution, Institute of Geology and Geophysics of the Chinese Academy of Science  
227 (Beijing, China). Zircons were analyzed using a Geolas-193 laser ablation coupled with a Neptune  
228 Multi-Collector Inductively Coupled-Plasma Mass-Spectrometer (MC-ICP-MS) as described in Wu  
229 et al. (2006). During analyses, isobaric interference of  $^{176}\text{Lu}$  on  $^{176}\text{Hf}$  was corrected assuming  
230  $^{175}\text{Lu}/^{176}\text{Lu} = 0.02655$ ; and the isobaric interference of  $^{176}\text{Yb}$  on  $^{176}\text{Hf}$  was corrected using the  
231 average fractionation index measured from the individual analysis proposed by Iizuka and Hirata  
232 (2005). Reference zircon 91500 ( $^{176}\text{Hf}/^{177}\text{Hf} = 0.282305$ , Wu et al., 2006) was used as a primary

233 standard for machine calibration, and also Mud Tank was used as a secondary reference material for  
234 data evaluation. During analyses, the obtained  $^{176}\text{Hf}/^{177}\text{Hf}$  value from Mud Tank is  $0.282521 \pm 16$   
235 (2SD,  $n=12$ ), which is consistent with the recommended value of  $0.282507 \pm 6$  (2SD,  $n=5$ ) within  
236 analytical uncertainty (Woodhead and Hergt, 2005). All of the Hf isotopic analyses were performed  
237 near the U-Pb spots, and the data are reported in Tab. 2. The calculation of  $\epsilon_{\text{Hf}}$  and depleted mantle  
238 model age ( $T_{\text{DM}}$ ) was done as in Wu et al. (2007).

239 The O isotope composition of pure separates of orthopyroxene (from MR01CR, FI09C04 and  
240 FI09C34 samples), clinopyroxene (FI09C04 and FI09C34 samples) and zircon (only from sample  
241 MR01CR) have been analyzed at the I.G.G.-C.N.R., Pisa by conventional laser fluorination (Sharp,  
242 1995) coupled with a Finnigan Delta Plus mass spectrometer. Analyses were performed following  
243 methods described by Perinelli et al. (2011). Results are reported in Tab. 3.

244

## 245 **Results**

246

### 247 *U-Pb zircon ages*

248 Separated zircons are anhedral to subhedral, inclusion-free, but locally fractured. Zircons from the  
249 Ol-chromitite are slightly pinkish, while those from the Opx-chromitites are colourless. All the  
250 separated zircons show low cathodoluminescence (CL). No internal zoning is shown by the Opx-  
251 chromitite zircons (Fig. 3) and by most of those from the Ol-chromitite. However, some Ol-  
252 chromitite zircons display two different, broad internal domains, the core being slightly darker (Fig.  
253 3). Most of the U-Pb LA-ICP-HRMS analyses of the zircons from Opx-chromitites provide Early  
254 Jurassic concordant U-Pb ages. The twenty-nine analyses from twenty-seven FI09C04 zircons  
255 provided twenty concordant ages varying from  $178 \pm 5$  to  $199 \pm 6$  Ma (Fig. 4), with a concordia  
256 ages of  $187 \pm 2$  Ma (95% confidence level error, MSWD=1.8; Fig. 5). The other single-spots show  
257 slightly discordant U-Pb data, but with  $^{206}\text{Pb}/^{238}\text{U}$  ages in the same interval defined by the  
258 concordant ages, with exception of zircon 33 showing a Late Triassic age ( $208 \pm 4$  Ma; Fig. 4).

259 Similarly, ten zircon grains from the FI09C34 sample yielded eight concordant ages ranging from  
260  $185 \pm 6$  to  $193 \pm 7$  Ma, with a concordia ages of  $187 \pm 1$  Ma (95% confidence level error, MSWD =  
261 3.2).

262 Most of the analyses of the MR01CR zircons (twenty-eight out of thirty) also give Lower Jurassic  
263 concordant ages ranging mainly from  $181 \pm 6$  to  $197 \pm 6$  Ma and providing a concordia age of  $188$   
264  $\pm 1$  Ma (95% confidence level error, MSWD = 2.0; Fig. 5). However, the darker internal domain of  
265 some zircons provide older ages, two of them giving Triassic (Anisian-Carnian) concordant ages at  
266  $242 \pm 7$  Ma and  $229 \pm 7$  Ma (Tab. 1; Fig. 3, 4).

267

#### 268 *Major and Trace Mineral chemistry*

269 Chromites from the investigated samples cover the same compositional field defined by those from  
270 other FPP chromitite layers documented by Grieco et al. (2001, 2004; Fig. 6). Chromites from the  
271 Opx-chromitites also approach the compositions of those from the phlogopite harzburgites-  
272 pyroxenites association (Siena and Coltorti, 1989; Zanetti et al., 1999; Grieco et al., 2001), whereas  
273 the Ol-chromites from Sasso Rosso show higher Cr#. The same behaviour is shown by the  
274 pyroxenes composition, with those from the Opx-chromitites possessing larger  $\text{Al}_2\text{O}_3$  contents (up  
275 to 1.3 wt.%), which approach those in the phlogopite harzburgites-pyroxenites association, while  
276 Ol-chromitite pyroxenes have a very Al-poor composition (0.6-0.1 wt.%  $\text{Al}_2\text{O}_3$ ). The increase of Al  
277 content in pyroxenes is accompanied by a significant decrease of Mg# of pyroxenes and olivine. As  
278 a whole, Mg# of pyroxenes and olivines in chromitite layers are distinctly higher than in the  
279 phlogopite harzburgites-pyroxenites association.

280 The clinopyroxene from the Opx-chromitites is strongly enriched in LREE with respect to MREE  
281 and HREE (Fig. 7;  $\text{La}_N/\text{Sm}_N$  between 3.09-5.26 and  $\text{La}_N/\text{Yb}_N$  between 21.43-42.47). The REE  
282 patterns are comparable with those of the clinopyroxene from the phlogopite harzburgite-pyroxenite  
283 association (SIMS analysis: Zanetti et al., 1999), but significantly different from those in late  
284 dolomite-apatite-wehrlites and apatite-orthopyroxenites and their host harzburgites (Zanetti et al.,

1999; Morishita et al., 2008). These relationships are also apparent by inspection of the PM-normalised spider diagrams (Primitive Mantle values from McDonough and Sun, 1995), in which the patterns of Opx-chromitite clinopyroxenes match considerably those of the phlogopite harzburgites-pyroxenites association, in particular sharing the very low Nb/LREE ratio, the positive Sr anomaly and the very large Sc/HREE ratio. The trace element concentration of amphibole in sample FI09C34 is strictly similar to those found in the country phlogopite harzburgites, as in the associated clinopyroxenites.

Zircons from Opx-chromitites show very similar trace elements composition. REE patterns are typically HREE-enriched, with La, Pr and Nd between 1-2 xCI (normalized to Chondrite I, CI: Lyubetskaya and Korenaga, 2007), a strong positive Ce anomaly (~10 xCI), and a steady enrichment from Sm to Lu (with maximum at Lu<sub>N</sub> from 36 to 53) with a slight negative Eu anomaly (Fig. 8). Th and U concentrations are both ~200 ppm: as a consequence the Th/U is ~1. Pb and Ti are ~6 and ~19 ppm, respectively.

Zircons from Ol-chromitite display REE patterns with the same La and Lu concentration of the Opx-chromitite ones (Fig. 8), but with slightly higher contents from Ce to Yb. Ce and Eu still determine positive and negative anomalies, respectively. Th and U are higher (~480 and ~670 ppm, respectively), with Th/U of ~0.7. Pb and Ti are 7-16 and 7-12 ppm, respectively.

In all the chromitite zircons, HREE and Y are distinctly lower than in the magmatic ones from the External Gabbro (Zanetti et al., 2013) and the nepheline diorite pegmatites (Schaltegger et al., 2015) of the Finero Complex.

305

#### 306 *Hf and O isotope composition*

307 The zircons from the three studied samples share similar Hf isotopic ratios. In particular,  $^{176}\text{Hf}/^{177}\text{Hf}$   
308 is between  $0.282486\pm 18$ - $0.282582\pm 16$  and  $0.282492\pm 18$ - $0.282587\pm 19$  for FI09C04 and FI09C34,  
309 respectively, with the weighted average values identical within uncertainty ( $0.282542\pm 11$ , MSWD

310 8.9, 95% conf. for FI09C04;  $0.282535 \pm 22$ , MSWD 9.7, 95% conf., for FI09C34). MR01CR zircons  
 311 have  $^{176}\text{Hf}/^{177}\text{Hf}$  between  $0.282550 \pm 12$ - $0.282610 \pm 13$  for, with a weighted average slightly higher  
 312 than that the Opx-chromitite zircons ( $0.282580 \pm 8$ , MSWD 7.9, 95% conf.). The calculated  $\epsilon\text{Hf}_{(188)}$   
 313 span from -5.9 to -1.6 (Fig. 9), with weighted average values of  $-3.9 \pm 0.4$  for FI09C04 (MSWD  
 314 7.6, 95% conf.),  $-4.2 \pm 0.8$  for FI09C34 (MSWD 9.7, 95% conf.), and  $-2.7 \pm 0.3$  for MR01CR  
 315 (MSWD 7.9, 95% conf.). Badanina et al. (2013), for zircons from FPP chromitite layers reported  
 316  $^{176}\text{Hf}/^{177}\text{Hf}$  values similar to those obtained in this study ( $^{176}\text{Hf}/^{177}\text{Hf}$  between 0.282533-0.282652  
 317 for ~90% of zircons).

318 Pyroxenes from Opx-Chromitites show very uniform O isotopic compositions, with positive  
 319 fractionation in orthopyroxene ( $\delta^{18}\text{O}$  is 6.5-6.7‰ for clinopyroxene, 6.8-6.9‰ for orthopyroxene;  
 320 Fig. 10). Zircons from Ol-chromitite exhibit comparable  $\delta^{18}\text{O}$  (6.8‰), but the associated  
 321 orthopyroxene has significantly lighter O isotopic composition (5.4‰). The  $\delta^{18}\text{O}$  of the pyroxenes  
 322 from Opx-chromitites and of the zircons from the Ol-chromitite are significantly higher than the  
 323 typical range defined by mantle lithologies and mantle-derived melts (5.5-5.9‰ and 5.8-6.2‰,  
 324 respectively; see Bindeman, 2008 and references therein), as well as of the values reported by  
 325 Selverstone and Sharp (2011) for a series of lithologies from the FPP, but they more closely match  
 326 the compositions found in FPP amphiboles and phlogopites by Hartmann and Wedephol (1993).



## 328 **Discussion**

### 329 *Concepts on the origin of chromitites*

330 Ferrario and Garuti (1990), Garuti et al. (1997), Grieco et al. (2001, 2004), Zaccarini et al. (2004)  
 331 propose models in which dunites formation and chromitites segregation were linked to the  
 332 pervasive metasomatism experienced by the FPP, but with significant differences in terms of both  
 333 series of processes and melt compositions.

334 In particular, Grieco et al. (2001) proposed that chromite layers and their dunite haloes formed by  
 335 interaction between basic melts and the ambient harzburgite. The residual melts of this process

336 invaded the country rock harzburgites, with precipitation of clinopyroxene and amphibole. In this  
337 scenario, phlogopite crystallisation was a successive event related to the late intrusion of  
338 clinopyroxenites, which induced K-metasomatism.

339 Zaccarini et al. (2004) concluded that chromitites and phlogopite metasomatism were the result of  
340 the interaction of uprising alkaline-carbonatitic fluids with the ambient harzburgite in the  
341 framework of mantle diapirism at the base of the continental crust induced by extensional tectonics.  
342 Our data place further constraints on the geochemical affinity of the chromitite parent melts, as well  
343 as on its compositional relationships with the metasomatic agent producing the phlogopite-  
344 harzburgite and pyroxenite association. The possible effects of the late melt migrations recorded by  
345 the FPP have to be evaluated, in particular in terms of zircon and pyroxenes  
346 crystallisation/recrystallisation. It has been now widely documented that mantle chromitites after  
347 their formation are particularly stable over a very large range of P-T-X conditions, and that they can  
348 record the migration of different melts/fluids (Howell et al., 2015), sometimes associated to the  
349 precipitation of zircons at mantle depths, over a very large time interval. This issue is relevant for  
350 the interpretation of the geochemical evolution of FPP chromitites, because they show some zoning  
351 of the mineral chemistry, and variations in the modal content of PGE minerals, which suggest  
352 possible interactions with late fluids/melts (Grieco et al., 2001, 2004).

353

#### 354 *Geochemical constraints on chromitites and zircons origin*

355 Several lines of evidence point to a strict geochemical affinity of the parent melts of the chromitite  
356 minerals with the metasomatic agents provoking the main metasomatic event of the FPP. First of  
357 all, this consideration is supported by the similarity of the major element composition of pyroxenes  
358 and spinels (in particular, in terms of very high Mg# and Cr/Al values; Fig. 6) and the evident  
359 consistency of the peculiar trace element compositions (i.e. enriched in Th, U and LREE, strongly  
360 depleted in HREE) of clinopyroxene and amphibole in the chromitites and in the phlogopite-  
361 harzburgites and pyroxenites association (Fig. 7). The similar geochemical affinity of chromitites

362 and harzburgites and pyroxenites is also supported by the similar trace element fractionation shown  
363 by the whole rock data reported by Grieco et al. (2001). The segregation of the chromitite zircons  
364 from the same parent melt is suggested by their REE composition. Compared to the magmatic  
365 zircons from the external gabbro and nepheline diorite pegmatites, they result enriched in LREE  
366 and markedly depleted in HREE, similar to zircons segregated from mantle-derived kimberlites to  
367 carbonatites (see Fig. 4 in Hoskin and Schaltegger, 2003). Even more stringent is the match of the  
368 peculiar, high  $\delta^{18}\text{O}$  of the chromitite pyroxenes with those of amphiboles and phlogopites from the  
369 phlogopite-harzburgites and pyroxenites association reported by Hartmann and Wedepohl (1993).  
370 The identical O isotopic composition of MR01CR zircons and Opx-chromitite pyroxenes suggests  
371 precipitation from a common parent melt. Although the  $\delta^{18}\text{O}$  partition coefficient between zircon  
372 and mafic phases is presently unconstrained, it has been widely documented that zircons segregated  
373 by mantle-derived melts show a very small  $\delta^{18}\text{O}$  interval at  $5.3 \pm 0.4$  (Valley et al., 2005;  
374 Bindeman, 2008; Tribuzio et al., 2014). A further valuable insight into the geochemical signature of  
375 the parent melts of the chromitite zircons and on the possible relationships with late melts migrating  
376 through the Finero Complex is provided by the zircon  $^{176}\text{Hf}/^{177}\text{Hf}$  ratios, which are much lower than  
377 the depleted mantle array. The  $\epsilon\text{Hf}_{(188)}$  values are sub-chondritic, at  $-6.1 \pm 0.6$  to  $-1.6 \pm 0.5$ ,  
378 consistent with the data by Badanina et al. (2013). This observation excludes any genetic  
379 relationship with the nepheline diorite pegmatites, whose zircons have  $\epsilon\text{Hf}_{(t)}$  between +6 to +9.8,  
380 evidence of segregation from mantle-derived melts (Schaltegger et al., 2015).  
381 The melts involved in the pervasive metasomatic event of the FPP, besides having high  $\delta^{18}\text{O}$  values,  
382 were characterised by isotopic composition of Nd, Sr, Pb, H, S, Cl and noble gases indicating the  
383 presence of “crustal” components (Hunziker and Zingg, 1982; Voshage et al., 1987, 1988;  
384 Cumming et al., 1987; Hartmann and Wedepohl, 1993; Obermiller, 1994; Seitz and Woodland,  
385 2000; Downes, 2001; Matsumoto et al., 2005; Selverstone and Sharp, 2011). The melt migration  
386 processes have been mainly attributed to supra-subduction environments (see among others Zanetti

387 et al., 1999; Grieco et al., 2001, 2004; Morishita et al., 2003, 2008; Matsumoto et al., 2005), but  
388 alternatively also to extensional settings (Garuti et al., 2001; Zaccarini et al., 2004).  
389 Negative  $\epsilon_{\text{Hf}}$  values are interpreted in the literature as the result of continental crust recycling (e.g.  
390 Belusova et al., 2004; Scherer et al., 2007; Lee et al., 2007; Wu et al., 2007). The presence of  
391 continental crustal component in the parent melts of chromitite is also strongly supported by the  
392 high  $\delta^{18}\text{O}$  zircon and by the large content in U and Th estimated for the parent melts by  
393 clinopyroxene composition and relevant clinopyroxene/liquid partition coefficients, but in particular  
394 by the occurrence of thorianite, thorite and uraninite (Zaccarini et al., 2004; this study).  
395 The occurrence of contrasting geochemical signatures in part suggesting oceanic crust derivation  
396 (Cumming et al., 1987; Selverstone and Sharp, 2011) may be tentatively interpreted as being related  
397 to heterogeneity of the melt source and/or changes in the proportion of melt sources through time.

398

#### 399 *FPP Chromitite segregation model*

400 Chromitites in dunite bodies are interpreted as late crystallization events of melts migrating into the  
401 dunite (Arai and Yurimoto, 1994; Arai, 1997). Such layers are common in dunites from supra-  
402 subduction zones, where chromite is basically associated to olivine. The formation of chromitite  
403 and surrounding dunite envelope is mainly explained as the result of the interaction between exotic  
404 melts and host harzburgite, in association with magma mixing (c.f. Zhou et al., 1994, 1996; Arai,  
405 1997). The reference model assumes that in the first stage, an exotic  $\text{SiO}_2$ -undersaturated melt,  
406 introduced into the ambient peridotite at low pressure, may selectively dissolve pyroxenes, as well  
407 as hydrous minerals, and precipitate olivine producing a replacive dunite envelope. This process  
408 would form a relatively Si-rich melt, according to the following reaction:  $\text{SiO}_2$ -poor melt +  
409 pyroxenes + hydrous phases  $\rightarrow$  olivine +  $\text{SiO}_2$ -rich melt. If the dunite channel is further supplied by  
410 the  $\text{SiO}_2$ -undersaturated primary melt, after mixing with the Si-rich melt, an over-saturation in  
411 spinel components (Cr+Al) takes place, leading to the isolated precipitation of spinel (c.f. Arai,  
412 1997).

413 Grieco et al. (2001, 2004) proposed that the FPP chromitites and their dunite haloes formed by the  
414 interaction between basic melts and the ambient peridotites, where the segregation of phlogopite  
415 pyroxenites resulting from successive events of melt migration, unrelated to the chromitites.  
416 Instead, Zaccarini et al. (2004) suggested that chromitite layers, dunite channels and phlogopite  
417 harzburgites were the result of migration of alkaline-carbonatitic melts.

418 By contrast, Zanetti et al. (1999) stressed that the widespread precipitation of newly-formed,  
419 magmatic orthopyroxene in both phlogopite harzburgites and pyroxenites pointed to a SiO<sub>2</sub>-  
420 saturation of the metasomatic melts related to the pervasive recrystallisation of the FPP. As a  
421 consequence, the formation of dunite bodies evidences peculiar variations in melt composition, with  
422 pulses of SiO<sub>2</sub>-undersaturated melts determining the virtually complete resorption of pyroxenes,  
423 amphibole and phlogopite in channels/bodies up to tens of meters across at relatively high, spinel-  
424 facies P conditions (see Mazzucchelli et al., 2009). The presence of dunite bodies both concordant  
425 to discordant with respect to the mantle foliation, as well as some geochemical changes shown by  
426 the magmatic minerals precipitated within dunites indicate that SiO<sub>2</sub>-undersaturated melts occurred  
427 in different stages of the FPP metasomatic cycle (Giovanardi, 2012).

428 The porphyroclastic textures of the Ol-chromitite MR01CR suggests that the development of  
429 structural weaknesses into the dunite bodies may have driven the migration and mixing of the  
430 different melt components. The presence of SiO<sub>2</sub>-saturated components in the parent melts is  
431 confirmed by the nearly ubiquitous presence of newly-formed orthopyroxene replacing olivine. In  
432 fact, this feature is present even in the first stages of chromitites formation solely characterised by  
433 chromite precipitation (in association to zircon and thorite as accessory mineral phases), as  
434 documented by Ol-chromitite MR01CR. The SiO<sub>2</sub>-saturation of the melt is more apparent in the  
435 Opx-chromitites, which record the complete recovery of the texture characterised by replacement of  
436 olivine by secondary orthopyroxene in textural equilibrium with chromite. These petrographic  
437 trends, along with the progressive chemical variation from the strongly refractory compositions of  
438 the Ol-chromitites to relatively Al-Fe-richer compositions in the Opx-chromitites, allow us to

439 suggest that the Opx-chromitites are related to levels that experienced the largest time-integrated  
440 chromitite melt/dunite ratios.

441 Two different processes may be envisaged to explain the strong presence of such a metasomatic  
442 component in the parent melts of chromitites. The first, according to the Arai's model, is the result  
443 of the dissolution of pyroxenes and hydrous minerals of the, already metasomatised, ambient  
444 harzburgites-pyroxenites association upon interaction with uprising of mafic melts. This is  
445 presumably the general process, always present in any FPP dunite body. However, the occurrence  
446 in some dunites of late phlogopite pyroxenites, rich in orthopyroxenes, strictly similar with those  
447 forming the main sequence (Grieco et al., 2001; Giovanardi, 2012) suggests that, at least locally,  
448 there might be mixing between mafic melts present in dunite channels and new upcoming SiO<sub>2</sub>-  
449 saturated melts bearing the continental crustal component. The mixing of these two components, at  
450 a new transition of the melt composition (i.e. from SiO<sub>2</sub>-undersaturated to SiO<sub>2</sub>-saturated), may  
451 have triggered the precipitation of some chromitites, followed by a segregation of pyroxenites  
452 within the dunite bodies.

453

#### 454 *Interpretation of the U-Pb ages*

455 The age of the petrologic processes recorded by the FPP is still controversial due to a very large  
456 time span documented by geochronological investigations, from the Early Permian to the Early  
457 Jurassic (Voshage et al., 1987, 1988; Stähle et al., 1990, 2001; Hartmann and Wedephol, 1993;  
458 Friedrichsen as cited by Hartmann and Wedephol, 1993; von Quadt et al., 1993; Grieco et al., 2001;  
459 Matsumoto et al., 2005; Morishita et al., 2008; Badanina et al., 2013; this work). Apparently late  
460 intrusive or metasomatic events (i.e. those documented by Stähle et al., 1990, 2001; the alkaline  
461 veins of Grieco et al., 2001; Matsumoto et al., 2005; Morishita et al., 2008) mainly provide Middle  
462 Triassic to Early Jurassic ages (from 240 Ma to 195 Ma). The Triassic to Early Jurassic U-Pb ages  
463 shown by chromitite zircons can be interpreted in two different ways: i) the record of Jurassic,

464 channelled melt migration with preservation of some Triassic relicts, or ii) the result of the  
465 perturbation of the U-Pb zircon systems at Early Jurassic.

466 The first scenario has some serious drawbacks, among which: 1) the abundance of Triassic to  
467 Permian ages of chromitite zircons from the FPP documented by Grieco et al. (2001) ( $208 \pm 2$  Ma),  
468 Badanina and Malitch (2012) and Badanina et al. (2013) ( $288 \pm 7$  Ma;  $249 \pm 3$  Ma;  $209 \pm 4$  Ma); 2)  
469 the Triassic age of late alkaline bodies discondatly cutting the harzburgite-pyroxenite association  
470 ( $225 \pm 13$  Ma; Stähle et al., 2001); 3) the Depleted Mantle geochemical affinity of the intrusives of  
471 the associate Finero Mafic Complex showing analogously Triassic to Early Jurassic radiometric  
472 data ( $231 \pm 23$  Ma to  $214 \pm 17$  Ma: Lu et al., 1997a,b;  $232 \pm 3$  Ma to  $214 \pm 5$  Ma: Zanetti et al.,  
473 2013; 212.5 and 190 Ma: Schaltegger et al. 2015). Moreover, the petrochemical observations  
474 reported in the previous sections clearly indicate that the chromitite zircons were segregated in the  
475 early metasomatic cycle producing the phlogopite harzburgites and pyroxenites association of FPP.  
476 Thus, it is here proposed that the different age clusters exhibited by the FPP chromitite zircons are  
477 the result of progressive re-equilibration stages of the U-Pb system at subsolidus condition.

478 This is consistent with the absence of CL zoning structures in most of the analyzed zircons of this  
479 study showing Early Jurassic ages. It is a common observation for mantle zircons, interpreted as the  
480 evidence of compositional homogenization due to a prolonged residence at high temperature in  
481 mantle conditions (Corfu et al., 2003).

482 The re-equilibration of the U-Pb system could most easily have occurred in fluid-assisted  
483 conditions. Currently no mineralogical or geochemical data support this hypothesis which, however,  
484 cannot be discarded.

485 In the framework depicted above, the  $288 \pm 7$  Ma age provided by the pinkish zircon population  
486 with internal oscillatory-zoning of Badanina et al. (2013) is a minimum age of the FPP pervasive  
487 metasomatism. Such an Early Permian age would relate the FPP pervasive metasomatism to the  
488 transtensional regime affecting the Variscan orogen, and associated to the formation of the Mafic

489 Complex of the Val Sesia-Type IVZ, with the emplacement of large volumes of mantle-derived  
490 tholeiitic melts at the bottom of the Adria crust (Zanetti et al., 2013 and references therein).

491 The peculiar composition of the metasomatic melts recorded by the FPP requires the concomitant  
492 mobilisation of deep-seated reservoirs containing continental crust component. It was possibly  
493 related to Variscan subduction of continental crust and metasomatism of the overlying mantle  
494 wedge by crustal-derived melts / fluids at ~330 Ma (e.g. Ulten Area, Eastern Alps: Tumietti et al.,  
495 2003; Sapienza et al., 2009; Langone et al., 2011).

496

497

498 *Evidence for peculiar P-T conditions of the Finero-Type IVZ*

499 According to the reference model of Quick et al. (1995), the mantle bodies of Val Sesia-Type IVZ  
500 were already intercalated into the crustal basement at least by the end of the Variscan orogeny,  
501 having been progressively incorporated in the cumulates of the underplated Mafic Complex during  
502 the Early Permian.

503 A pronounced re-equilibration of the U-Pb zircon system similar to that shown by chromitite  
504 zircons has so far not been documented in the deepest rocks of the Val Sesia-Type IVZ. In  
505 particular, although zircons have never been found in associated mantle lithologies, they are  
506 common in the gabbroic rocks of the Mafic Complex documenting processes down to 25 km depth  
507 (i.e. ~0.8 GPa; Demarchi et al., 1998). Detailed inspections of magmatic zircons from the Mafic  
508 Complex performed by Peressini et al. (2007) evidenced the dominant presence of Early Permian  
509 ages, with only one Mesozoic age (180 Ma) given by a single-spot on recrystallised “white pest”  
510 rim. Consistently, up-to-date reconstructions of the thermal evolution of the polymetamorphic  
511 Kinzigite Formation of the IVZ do not provide evidence that the rifting of the Adriatic margin  
512 during the Early Jurassic induced conditions capable to reset the U-Pb system in zircon and  
513 monazite placed at crustal levels (Handy et al., 1999; Smye and Stockli, 2014; Ewing et al., 2015).  
514 Locally, fluid-assisted partial recrystallization of zircon domains at ~220-200 Ma characterises

515 some IVZ metapelites of the Kinzigite Formation in the transitional zone between Val Sesia-Type  
516 IVZ and Finero-Type IVZ (Vavra et al., 1999; Ewing et al., 2013), presumably as a consequence of  
517 documented Late Triassic magmatism and of the related fluid activity. Vavra and Schaltegger  
518 (1999) also observed that monazites from the Kinzigite Formation yield a subconcordant discordia  
519 line with a lower intercept age of  $210 \pm 14$  Ma, interpreted as an episode of fluid-driven Pb loss  
520 associated with the influx of hydrothermal fluids.

521 Thus, it is here speculated that the prolonged re-equilibration of the U-Pb system displayed by  
522 chromitite zircons must be associated to peculiar P-T conditions affecting the FPP, such as  
523 permanence at great (mantle) depths, possible till the Early Jurassic, and/or a reheating phase due to  
524 a later (Early Jurassic) tectono-magmatic activity.

525 The residence of the FPP at relatively high pressure up to Mesozoic time is supported by the  
526 presence of magmatic sapphirine in one of the late, if not the last, magmatic intrusions represented  
527 by apatite-calcite-bearing gabbroic dyke swarms, discordantly cutting all the other rocks and  
528 structures of the FPP. The precipitation of magmatic sapphirine in gabbroic rocks is consistent with  
529 pressures above than 1.1 GPa (Giovanardi et al., 2013). In particular, the composition of sapphirine-  
530 saturated melts corresponds to basalt to andesite at pressures of 1.1–1.5 GPa, and the stability field  
531 of the magmatic sapphirine extends to  $P > 3$  GPa (Milholland and Presnall, 1999). Equilibrium  
532 pressures exceeding those at the bottom of the Mafic Complex of the Val Sesia-Type IVZ (i.e. 0.8  
533 GPa), have been also estimated for the Finero Mafic Complex by Siena and Coltorti (1989) at  $\sim 1.0$   
534 GPa (at  $\sim 1000^\circ\text{C}$ ). Accordingly, Sills et al. (1983) and Christy (1989) estimated 0.9-1.1 GPa (at T  
535 of  $800\text{--}950^\circ\text{C}$ ) for the subsolidus reaction involving formation of metamorphic sapphirine in the  
536 gabbroic lithologies of LIZ.

537 The development of regional thermal positive perturbations in the northern part of the IVZ, possibly  
538 associated to asthenosphere upwelling, can be inferred from the Triassic to the Early Jurassic cycles  
539 of magmatic activity segregating zircons. This hypothesis is consistent with the high temperature  
540 conditions (granulite-facies) argued for the lower IVZ by Brodie and Rutter (1987) in proximity of

541 the Anzola-Val Grande shear zone during the Middle to Late Triassic. It is also indirectly supported  
542 by the change of the metamorphic conditions along the Pogallo Line, governed by brittle  
543 deformation to the south of Val d'Ossola, and by ductile deformation to the north (Handy, 1987).  
544 The temperatures recorded by the cooling paths along the Pogallo Line are consistently higher in  
545 the northern than in the southern sector of the IVZ (Wolff et al., 2012).

546  
547 *Constraints on the Mesozoic geodynamic evolution of Finero-Type IVZ*

548 Geochronological data supports multiple melt injections throughout the Triassic to Early Jurassic in  
549 the Finero-Type IVZ (Zanetti et al., 2013 and references therein). The reappraisal of all data  
550 available suggests that a first magmatic stage was dominated by segregation of gabbroic to  
551 anorthositic rocks from ~240 to 230 Ma (Gebauer, 1993; Hingerl et al., 2008; Zanetti et al., 2013),  
552 possibly associated to the emplacement of anatectic granites in the Kinzigite Formation adjacent to  
553 the Finero Complex at  $242 \pm 3$  Ma (Vignola et al., 2008), matching the oldest age found in the core  
554 of zircons from MR01CR ( $242 \pm 7$  Ma). Volcanic activity also formed (241-238 Ma)  
555 porphyroclastic intercalations in the pelagic succession of the western Southern Alps (Mundil et al.,  
556 1996). A second main stage was characterised by the intrusion of nepheline diorite pegmatites at  
557 225-190 Ma (Klötzli et al., 2007, 2009; Schaltegger et al., 2015). A Late Triassic magmatic event in  
558 the FPP is recorded by the emplacement of apatite-carbonate-bearing alkaline diorite and  
559 hornblendite dykes at 225-220 Ma and probably also apatite-carbonate-bearing orthopyroxenite  
560 veins ( $240 \pm 41$  Ma, phlogopite Ar-Ar (Matsumoto et al. 2005) and  $213 \pm 35$  Ma, apatite U-Pb  
561 (Morishita et al., 2008).

562 The occurrence of anomalous heating processes at a regional scale has been confirmed by several  
563 papers dealing with cooling ages of the IVZ and adjacent area (Wolff et al. 2012; Smye and Stockli,  
564 2014; Ewing et al., 2013, 2015; Beltrando et al., 2015). In particular, Beltrando et al. (2015)  
565 document the progressive westward rejuvenation of (U-Th)/(He) ages (hereafter ZHe ages), from  
566 280-240 Ma in the Lombardian basin to 215-200 Ma near the Sostegno and Fenera basins,

567 indicating that anomalously high thermal gradients were established in the Late Triassic towards the  
568 area where the actual rifting of Alpine Tethys was later localized. This suggests that rift localization  
569 along the western margin of the Adriatic plate was probably favoured by a lithospheric thermal  
570 anomaly, established at 215-210 Ma, followed by thermal decay at 200-190 Ma (Ewing et al., 2013,  
571 2015; Beltrando et al., 2015).

572 The Early Jurassic (~200-180 Ma) age interval provided by most of the zircons from the FPP  
573 chromitites broadly corresponds to the final stages of extensional faulting as recorded in the IVZ by  
574 the Pogallo Line, which was active between 210 and 170 Ma (Zingg et al., 1990), and the Anzola-  
575 Val Grande high-T shear zone (Brodie and Rutter, 1987; Brodie et al., 1989), whose movement is  
576 considered to have spanned the period between 230-180 Ma. It also matches the final stages of  
577 development of the Lombardian Basin at ~220-180 Ma (Bertotti et al., 1999 and references therein),  
578 located just east of the IVZ. Although the geodynamic setting of the Middle Triassic deformation  
579 stages of the IVZ is still debated (see Zanetti et al., 2013), there is a wide consensus that the Late  
580 Triassic-Early Jurassic deformation phases was a precursor events of the opening of the Alpine  
581 Tethys, which involved crustal thinning, mantle exhumation and a partial rotation of the IVZ (15° to  
582 23° of tilting; Wolff et al., 2012). It is thus proposed that the age interval shown by colourless  
583 smoky chromitite zircons and, in particular, the closure of the U-Pb system of the mantle zircons at  
584 ~180 Ma, document the exhumation stage of the FPP.

585 Smye and Stockli (2014) evidenced that the IVZ underwent a reheating event of sufficient duration  
586 and T to reset the U-Pb system of rutile in granulites of the Kinzigite Formation at ~180-190 Ma,  
587 possibly due to hyperextension of the Adriatic lithosphere. An Early Jurassic heating has been also  
588 invoked to explain the resetting of the ZHe thermochronometer in the Baveno granite (Wolff et al.,  
589 2012). Subsequent crust-wide extension led to breakup of continental crust and mantle exhumation.  
590 ZHe ages in detrital zircons from syn-tectonic sandstone constrain the onset of normal faulting in  
591 the axial zone at 185-180 Ma (Beltrando et al., 2015). It is thus concluded that the ages shown by  
592 FPP chromitite zircons record thermal perturbations in the Triassic-Early Jurassic time span, the

593 youngest one reflecting hyperextension of the Adriatic lithosphere (Smye and Stockli, 2014), and  
594 regional Early Jurassic magmatic activity (Mazzucchelli et al., 2010; Schaltegger et al., 2015). The  
595 absence of evidence for partial melting in the FPP suggests that such thermal perturbations never  
596 exceeded 965°C, which is the solidus temperature estimated for the Finero phlogopite harzburgites  
597 (Giovanardi et al., 2013).

598

### 599 **Concluding Remarks**

600 Field relationships, the major element composition of spinel and pyroxenes, the trace element  
601 composition of clinopyroxene and zircon, the O isotopic composition of zircon and pyroxenes, and  
602 the Hf isotopic composition of zircon converge in indicating that the chromitite layers here studied  
603 were segregated from hybrid melts derived from the mantle but strongly contaminated by continental  
604 crust.

605 The FPP chromitite zircons yield ages spanning the Early Permian to the Early Jurassic, interpreted  
606 as indicating primary crystallization in the Early Permian and resetting during thermal disturbances  
607 in the Jurassic. The chromitite zircon data indicate that the FPP was at mantle depths since the  
608 Early Permian, being exhumed at shallower, crustal levels only during Early Jurassic. The youngest  
609 event appears to have been connected to initiation of continental rifting and mantle exhumation,  
610 precursor events of the opening of the Alpine Tethys. Our data, along with those of Grieco et al.  
611 (2001), Badanina and Malitch (2012) and Badanina et al. (2013), support that lithosphere rifting and  
612 exhumation were affected by two strong thermal perturbations at 208 Ma and 187 Ma.

613 In our model for the northern IVZ, the pervasive metasomatism of the FPP occurred ~290 Ma  
614 and/or before. However, the possibility that the actual age of pervasive metasomatism of FPP was  
615 older and related to the Variscan orogenic cycle cannot be excluded.

616

### 617 **Acknowledgements**

618 This study is part of the investigations carried out in the frame of the XXV<sup>o</sup> cycle of PhD degree  
619 awarded by the Doctorate School in Science and Technology, University of Pavia.

620 Tomoaki Morishita, Yumiko Harigane, and Takahito Suzuki are deeply thanked for their assistance  
621 during the field work and the samples collection.

622 We want to thank the two reviewers, Fernando Corfu and Urs Klötzli, for their stimulating and  
623 constructive reviews that allowed a significant improvement of the manuscript.

624 The paper benefited of the Research Support Foundation of the State of São Paulo (FAPESP), in the  
625 frame of project 2013/19519-6.

626

627

#### 628 **Supplementary Material Captions**

629 Table A: Major-element composition of mineral phases as wt.% and a.p.f.u. Formulae.

630 Table B: Trace-element compositions of zircons, clinopyroxenes and amphiboles in ppm and  
631 single-analysis elements detection limits.

632 Supplementary Material C: SEM images and EDS analysis of thorite in sample MR01CR.

633

#### 634 **References**

635 Arai, S., Yurimoto, H., 1994. Podiform chromitites of the Tari-Misaka ultramafic complex,

636 southwestern Japan, as mantle-melt interaction products. *Economic Geology* 89(6), 1279-1288.

637 Arai, S., 1997. Origin of podiform chromitites. *Journal of Asian Earth Sciences* 15(2-3), 303-310.

638 Badanina, I.Yu., Malitch, K.N., 2012. Timing of metasomatism in a subcontinental mantle:

639 evidence from zircon at Finero (Italy). *Geophysical Research Abstracts* 14, EGU2012-7304-1.

640 Badanina, I.Yu., Malitch, K.N., Belousova, A., 2013. U-Pb and Hf isotope characteristics of zircon

641 from chromitites at Finero. *Goldschmidt2013 Conference Abstracts*, 639.

- 642 Belusova, E.A., Griffin, W.L., O'Reilly, S.Y., 2004. Zircon crystal morphology, trace element  
643 signature and Hf isotope composition as a tool for petrogenetic modelling: examples from eastern  
644 Australia granitoids. *Journal of Petrology* 47, 329-353.
- 645 Beltrando, M., Stockli, D.F., Decarlis, A., Manatschal, G., 2015. A crustal-scale view at rift  
646 localization along the fossil Adriatic margin of the Alpine Tethys preserved in NW Italy. *Tectonics*,  
647 34/9, 1927-1951.
- 648 Bertotti, G., Seward, D., Wijbrans, J., Voorde, M.ter, Hurford, A.J., 1999. Crustal thermal regime  
649 prior to, during, and after rifting: A geochronological and modeling study of the Mesozoic South  
650 Alpine rifted margin. *Tectonics* 18(2), 185-200.
- 651 Bindeman, I., 2008. Oxygen Isotopes in Mantle and Crustal Magmas as Revealed by Single Crystal  
652 Analysis. *Reviews in Mineralogy and Geochemistry* 69, 445-478.
- 653 Blichert-Toft, F., Albarede, F., 1997. The Lu–Hf isotope geochemistry of chondrites and the  
654 evolution of the mantle–crust system. *Earth Planetary Science Letters* 148, 243-258
- 655 Brodie, K.H., Rutter, E.H., 1987. Deep crustal extensional faulting in the Ivrea Verbano Zone of  
656 Northern Italy. *Tectonophysics* 140, 193-212.
- 657 Brodie, K.H., Rex, D., Rutter, E.H., 1989. On the age of deep crustal extensional faulting in the  
658 Ivrea Zone, Northern Italy. In: Coward, M.P., Dietrich, D., Park, R.G. (Eds), *Alpine Tectonics*,  
659 Geological Society London, Special Publications 45, pp. 203-210.
- 660 Cawthorn, R.G., 1975. The amphibole peridotite - metagabbro complex, Finero, northern Italy.  
661 *Journal of Geology* 83, 437-454.
- 662 Christy, A.G., 1989. The stability of sapphirine + clinopyroxene: implications for phase relations in  
663 the CaO-MgO-Al<sub>2</sub>O<sub>3</sub>-SiO<sub>2</sub> system under deep-crustal and upper mantle conditions. *Contributions*  
664 *to Mineralogy and Petrology* 102, 422-428
- 665 Coltorti, M., Siena, F., 1984. Mantle tectonite and fractionate peridotite at Finero (Italian Western  
666 Alps). *Neues Jahrbuch für Mineralogie - Abhandlungen* 149, 225-244.

- 667 Corfu, F., Hanchar, J.M., Hoskin, P.W.O., Kinny, P., 2003. Atlas of zircon textures. In: Hanchar,  
668 J.M., Hoskin, P.W.O. (Eds.), *Zircon. Reviews in Mineralogy and Geochemistry* 53, 469-500.
- 669 Cumming, G.L., Koeppel, V., Ferrario, A., 1987. A lead isotope study of the northeastern Ivrea  
670 Zone and the adjoining Ceneri Zone (N Italy): Evidence for a contaminated subcontinental mantle.  
671 *Contributions to Mineralogy and Petrology* 97, 19-30.
- 672 Demarchi, G., Quick, J.E., Sinigoi, S., Mayer, A., 1998. Pressure gradient and original orientation  
673 of a lower-crustal intrusion in the Ivrea-Verbano Zone, Northern Italy. *Journal of Geology* 106(5),  
674 609-622.
- 675 Downes, H., 2001. Formation and Modification of the Shallow Sub-continental Lithospheric  
676 Mantle: a Review of Geochemical Evidence from Ultramafic Xenolith Suites and Tectonically  
677 Emplaced Ultramafic Massifs of Western and Central Europe. *Journal of Petrology* 42 (1), 233-250.
- 678 Ewing, T.A., Rubatto, D., Hermann, J., 2013. The robustness of the Zr-in rutile and Ti-in-zircon  
679 thermometers during high-temperature metamorphism (Ivrea-Verbano Zone, northern Italy).  
680 *Contribution to Mineralogy and Petrology* 165, 757-779.
- 681 Ewing T.A., Rubatto D., Beltrando M., Hermann J., 2015. Constraints on the thermal evolution of  
682 the Adriatic margin during Jurassic continental break-up: U-Pb dating of rutile from the Ivrea-  
683 Verbano Zone, Italy. *Contribution to Mineralogy and Petrology* 169, p. 44. DOI 10.1007/s00410-  
684 015-1135-6
- 685 Ferrario, A., Garuti, G., 1990. Platinum-group mineral inclusions in chromitites of the Finero  
686 mafic-ultramafic complex (Ivrea-Zone, Italy). *Mineralogy and Petrology* 41, 125-143.
- 687 Garuti, G., Oddone, M., Torres, R.J., 1997. Platinum group-element distribution in subcontinental  
688 mantle: evidence from the Ivrea Zone (Italy) and the Betic-Rifean Cordillera (Spain and Morocco).  
689 *Canadian Journal of Earth Sciences* 34, 444-463.
- 690 Gebauer, D., 1993. Pre-Mesozoic geology in the Alps. In: von Raumer, J. F., Neubauer, F. (Eds),  
691 *The Pre-Alpine evolution of the continental crust of the Central Alps: an overview*. Springer-  
692 Verlag. pp. 93-117.

- 693 Giovanardi, T., 2012. Petrological, Geochemical and Geochronological constraints on the  
694 geodynamic evolution of the basic-ultrabasic sequence of Finero (Western Southern Alps).  
695 Unpublished PhD Thesis. Department of Earth and Environmental Sciences. pp. 154.
- 696 Giovanardi, T., Morishita, T., Zanetti, A., Mazzucchelli, M., Vannucci, R., 2013. Igneous  
697 sapphirine as a product of melt-peridotite interactions in the Finero Phlogopite-Peridotite Massif,  
698 Western Italian Alps. *European Journal of Mineralogy* 25, 17-31.
- 699 Giovanardi, T., Mazzucchelli, M., Zanetti A., Langone, A., Tiepolo, M., Cipriani, A., 2014.  
700 Occurrence of phlogopite in the Finero Mafic layered complex. *Open Geosciences*, 6(4), 588–613.
- 701 Grieco, G., Ferrario, A., von Quadt, A., Köppel, V., Mathez, A., 2001. The zircon-bearing  
702 chromitites of the phlogopite peridotite of Finero (Ivrea Zone, Southern Alps): evidence and  
703 geochronology of a metasomatized mantle slab. *Journal of Petrology* 42(1), 89-101.
- 704 Grieco, G., Ferrario, A., Mathez, E.A., 2004. The effect of metasomatism on the Cr-PGE  
705 mineralization in the Finero Complex, Ivrea Zone, Southern Alps. *Ore Geology Reviews* 24, 299-  
706 314.
- 707 Griffin, W.L., Pearson, N.J., Belousova, E., Jackson, S.E., van Acherbergh, E., O'Reilly, S.Y.,  
708 Shee, S.R., 2000. The Hf isotope composition of cratonic mantle: LAM-MC-ICPMS analysis of  
709 zircon megacrysts in kimberlites. *Geochimica et Cosmochimica Acta* 64, 133–147.
- 710 Handy, M.R., 1987. The structure, age and kinematics of the Pogallo fault zone - Southern Alps,  
711 northwestern Italy. *Eclogae Geologicae Helvetiae* 80, 593–632.
- 712 Handy, M., Franz, L., Heller, F., Janott, B., Zurbriggen, R., 1999. Multistage accretion, orogenic  
713 stacking, and exhumation of continental crust (Ivrea crustal section, Italy and Switzerland).  
714 *Tectonics* 18, 1154-1177.
- 715 Hartmann, G., Wedepohl, K.H., 1993. The composition of peridotite tectonites from the Ivrea  
716 Complex, northern Italy: Residues from melt extraction. *Geochimica et Cosmochimica Acta* 57,  
717 1761-1782.

- 718 Horstwood, M.S.A., Foster, G.L., Parrish, R.R., Noble, S.R., Nowell, G.L., 2003. Common-Pb  
719 corrected in situ U–Pb accessory mineral geochronology by LA-MC-ICP-MS. *Journal of Analytical*  
720 *Atomic Spectrometry* 18, 837-846.
- 721 Hoskin, P.W.O., Schaltegger, U., 2003. The composition of zircon and igneous and metamorphic  
722 petrogenesis. In: Hanchar, J.M., Hoskin, P.W.O. (Eds), *Zircon. Reviews in Mineralogy and*  
723 *Geochemistry* 53, 27–62.
- 724 Hingerl, F., Klötzli, U., Steuber, C., Kleinschrodt, R., 2008. New results from the mafic complex in  
725 the Finero area. 33<sup>th</sup> International Geological Congress, Oslo 6-14<sup>th</sup>, August 2008, *CD-ROM*  
726 *abstracts*, X-CD Technologies, <http://www.cprm.gov.br/33IGC/1344964.html>
- 727 Howell, D., Griffin, W.L., Yang, J., Gain, S., Stern, R.A., Huang, J.-X., Jacob, D.E., Xu, X., Stokes,  
728 A.J., O'Reilly, S.Y., Pearson, N.J., 2015. Diamonds in ophiolites: Contamination or a new diamond  
729 growth environment? *Earth and Planetary Science Letters* 430, 284–295.
- 730 Hunziker, J., Zingg, A., 1982. Zur genese der ultrabasischen gesteine der Ivrea-Zone. *Schweiz.*  
731 *Mineral. Petr. Mitt.* 62, 483-486.
- 732 Iizuka, T., Hirata, T., 2005. Improvements of precision and accuracy in in-situ Hf isotope  
733 microanalysis of zircon using the laser ablation-MC-ICPMS technique. *Chemical Geology* 220,  
734 121-137.
- 735 Ketchum, J.W.F., Jackson, S.E., Barr, S.M., Culshaw, N.G., 2001. Age, petrochemistry, and  
736 tectonic setting of the Paleoproterozoic Lower Aillik Group, Makkovik Province, Canada:  
737 evolution of a passive margin – foredeep sequence based on U–Pb (TIMS and LAM-ICP-  
738 MS) geochronology. *Precambrian Research* 105, 331-356.
- 739 Klötzli, U., Hochleitner, R., Kosler, J., 2007. Lower Triassic mantle-derived magmatism in the  
740 Ivrea-Verbano Zone: evidence from laser ablation U-Pb dating of a pegmatite from the eastern  
741 Finero Complex (Switzerland). *Mitteilungen der Österreichischen Mineralogischen Gesellschaft*,  
742 153.

- 743 Klötzli, U., Klötzli, E., Günes, Z., Kosler, J., 2009. Accuracy of Laser Ablation U-Pb Zircon  
744 Dating: Results from a Test Using Five Different Reference Zircons. *Geostandards and*  
745 *Geoanalytical Research* 33(1), 5-15.
- 746 Langone, A., Braga, R., Massonne, H.J., Tiepolo, M. (2011). Preservation of old (prograde  
747 metamorphic) U-Th-Pb ages in unshielded monazite from the high-pressure paragneisses of the  
748 Variscan Ulten Zone (Italy). *Lithos* (DOI: 10.1016/j.lithos.2011.08.007)
- 749 Langone, A., Tiepolo, M., (2015). U-Th-Pb “multi-phase” approach to the study of crystalline  
750 basement: application to the northernmost sector of the Ivrea-Verbano Zone (Alps). *Periodico di*  
751 *Mineralogia* (2015), 84, 3B (Special issue), xx-xx DOI: 10.2451/2015PM00xx
- 752 Lee, S.R., Cho, D.L., Cho, M., Wu, F.Y., Kim, H., Jeon, H., 2007. Hf isotopic evidence for  
753 Paleoproterozoic (>3.5 Ga) crustal components in the Korean Peninsula. *Geosciences Journal* 11, 271-  
754 277.
- 755 Lu, M., Hofmann, A.W., Mazzucchelli, M., Rivalenti, G., 1997a. The mafic-ultramafic complex  
756 near Finero (Ivrea-Verbano zone), I. Chemistry of MORB-like magmas. *Chemical Geology* 140,  
757 207-222.
- 758 Lu, M., Hofmann, A.W., Mazzucchelli, M., Rivalenti, G., 1997b. The mafic-ultramafic complex  
759 near Finero (Ivrea-Verbano zone), II. Geochronology and isotope geochemistry. *Chemical Geology*  
760 140, 223-235.
- 761 Lyubetskaya, T., Korenaga, J., 2007. Chemical composition of Earth’s primitive mantle and its  
762 variance: 1. Method and results. *Journal of Geophysical Research* 112, B03211,
- 763 Ludwig, K.R., 2003. User’s manual for ISOPLOT/Ex 3.00, a geochronological toolkit for Microsoft  
764 Excel. Berkeley Geochronology Center, Special Publication 4, p. 70.
- 765 Mundil, R., Brack, P., Meier, M., Rieber, H. and Oberli, F., 1996. High resolution U-Pb dating of  
766 Middle Triassic volcanoclastics: Time-scale calibration and verification of tuning parameters for  
767 carbonate sedimentation. *Earth and Planetary Science Letters* 141, 137-151.

- 768 Mazzucchelli, M., Rivalenti, G., Brunelli, D., Zanetti, A., Boari, E., 2009. Formation of highly  
769 refractory dunite by focused percolation of pyroxenite-derived melt in the Balmuccia peridotite  
770 massif (Italy). *Journal of Petrology* 50, 1205-1233.
- 771 Mazzucchelli, M., Zanetti, A., Rivalenti, G., Vannucci, R., Correia, C.T., Tassinari, C.C.G., 2010.  
772 Age and geochemistry of mantle peridotites and diorite dykes from the Baldissero body: Insights  
773 into the Paleozoic-Mesozoic evolution of the Southern Alps. *Lithos* 119, 485-500.
- 774 Mazzucchelli, M., Quick, J.E., Sinigoi, S., Zanetti, A., Giovanardi, T., 2014. Igneous evolutions  
775 across the Ivrea crustal section: the Permian Sesia Magmatic System and the Triassic Finero  
776 intrusion and mantle. *Goldschmidt Conference – Florence, 2013. Geological field trips*, 6(2.2). pp.  
777 98. DOI: 10.3301/GFT.2014.05, ISSN: 2038-4947
- 778 Matsumoto, T., Morishita, T., Masuda, J., Fujioka, T., Takebe, M., Yamamoto, K., Arai, S., 2005.  
779 Noble gases in the Finero Phlogopite–Peridotites, Italian Western Alps. *Earth and Planetary Science*  
780 *Letters* 238, 130–145.
- 781 Miller, C., Zanetti, A., Thöni, M., Konzett, J., Klötzli, U., 2012. Mafic and silica-rich glasses in  
782 mantle xenoliths from Wau-en-Namus, Libya: Textural and geochemical evidence for peridotite–  
783 melt reactions. *Lithos* 128-131, 11-26.
- 784 Milholland, C.S., Presnall, D.C., 1999. Liquidus phase relations in the CaO-MgO-Al<sub>2</sub>O<sub>3</sub>-SiO<sub>2</sub>  
785 system at 3.0 GPa: the Aluminous pyroxene thermal divide and high-pressure fractionation of  
786 picritic and komatiitic magmas. *Journal of Petrology* 39, 3–27.
- 787 Morishita, T., Arai, S., Tamura, A., 2003. Petrology of an apatite-rich layer in the Finero  
788 phlogopite–peridotite, Italian Western Alps; implications for evolution of a metasomatising agent.  
789 *Lithos* 69, 37-49.
- 790 Morishita, T., Hattori, K.H., Terada, K., Matsumoto, T., Yamamoto, K., Takebe, M., Ishida, Y.,  
791 Tamura, A., Arai, S., 2008. Geochemistry of apatite-rich layers in the Finero phlogopite–peridotite  
792 massif (Italian Western Alps) and ion microprobe dating of apatite. *Chemical Geology* 251, 99–111.

- 793 Nowell, G.M., Kempton, P.D., Noble, S.R., Fitton, J.G., Saunders, A.D., Mahoney, J.J., Taylor,  
794 R.N., 1998. High precision Hf isotope measurements of MORB and OIB by thermal ionisation  
795 mass spectrometry: insights into the depleted mantle. *Chemical Geology* 149, 211-233.
- 796 Obermiller, W.A., 1994. Chemical and isotopic variations in the Balmuccia, Baldissero and Finero  
797 peridotite massifs (Ivrea-Zone, N-Italy). Unpublished PhD thesis, Johannes Gutenberg-Universität  
798 Mainz, pp. 191.
- 799 Oppizzi, P., Schaltegger, U., 1999. Zircon bearing plagioclases from the Finero complex (Ivrea  
800 zone): dating a Late Triassic mantle hic-cup?. *Schweizerische Mineralogische und Petrographische*  
801 *Mitteilungen* 79, 330-331.
- 802 Peressini, G., Quick, J.E., Sinigoi, S., Hofmann, A.W., Fanning, M., 2007. Duration of a Large  
803 Mafic Intrusion and Heat Transfer in the Lower Crust: a SHRIMP U/Pb Zircon Study in the Ivrea-  
804 Verbano Zone (Western Alps, Italy). *Journal of Petrology* 48, 1185-1218.
- 805 Perinelli, C., Armienti, P., Dallai, L., 2011. Thermal Evolution of the Lithosphere in a Rift  
806 Environment as Inferred from the Geochemistry of Mantle Cumulates. Northern Victoria Land,  
807 Antarctica. *Journal of Petrology* 52(4), 665-690.
- 808 Quick, J.E., Sinigoi, S., Mayer, A., 1995. Emplacement of mantle peridotite in the lower continental  
809 crust, Ivrea-Verbano Zone, northwest Italy. *Geology* 23(8), 739-742.
- 810 Quick, J. E., Sinigoi, S., Peressini G., Demarchi, G., Wooden, J., Sbisà, A., 2009. Magmatic  
811 plumbing of a large Permian caldera exposed to a depth of 25 kilometers. *Geology* 3(7), 603-606.
- 812 Raffone, N., Le Fèvre, B., Ottolini, L., Vannucci, R., Zanetti, A., 2006. Light-Lithophile Element  
813 Metasomatism of Finero Peridotite (W ALPS): A Secondary-Ion Mass Spectrometry Study.  
814 *Microchimica Acta* 155, 251-255.
- 815 Rivalenti, G., Garuti, G., Rossi, A., Siena, F., Sinigoi, S., 1981. Existence of different peridotite  
816 types and of a layered igneous complex in the Ivrea Zone of the Western Alps. *Journal of Petrology*  
817 22, 127-153.

- 818 Rivalenti, G., Mazzucchelli, M., Vannucci, R., Hofmann, A. W., Ottolini, L., Bottazzi, P. and  
819 Obermiller, W., 1995. The relationship between websterite and peridotite in the Balmuccia  
820 peridotite massif (NW Italy) as revealed by trace element variations in clinopyroxene. *Contributions*  
821 *to Mineralogy and Petrology* 121, 275-288.
- 822 Rivalenti, G., Mazzucchelli M., 2000. Interaction of mantle derived magmas and crust in the Ivrea-  
823 Verbano Zone and the Ivrea mantle peridotites. In: Ranalli G., Ricci C.A. and Trommsdorff V.  
824 (Eds.). *Crust Mantle Interactions, Proceedings of the International School Earth and Planetary*  
825 *Sciences*, pp. 153-198.
- 826 Rutter, E., Brodie, K., James, T., Burlini, L., 2007. Large-scale folding in the upper part of the  
827 Ivrea-Verbano zone, NW Italy. *Journal of Structural Geology* 29, 1-17.
- 828 Sapienza, G.T., Scambelluri, M., Braga R., 2009. Dolomite-bearing orogenic garnet peridotites  
829 fitness fluid-mediated carbon recycling in a mantle wedge (Ulten Zone, Eastern Alps, Italy).  
830 *Contributions to Mineralogy and Petrology* 158, 401–420.
- 831 Schaltegger U., Ulianov A., Muntener O., Ovtcharova M., Peytcheva I., Vonlanthen P., Vennemann  
832 T.W., Antognini M., Girlanda F., 2015. Megacrystic zircon with planar fractures in miaskite-type  
833 nepheline pegmatites formed at high pressures in the lower crust (Ivrea Zone, southern Alps,  
834 Switzerland). *American Mineralogist* 100, 83-94.
- 835 Scherer, E.E., Whitehouse, M.J., Münker, C., 2007. Zircon as a monitor of crustal growth. *Elements*  
836 3(1), 19-24.
- 837 Seitz, H.M., Woodland, A.B., 2000. The distribution of lithium in peridotitic and pyroxenitic  
838 mantle lithologies — an indicator of magmatic and metasomatic processes. *Chemical Geology* 166,  
839 47–64.
- 840 Selverstone, J., Sharp, Z.D., 2011. Chlorine isotope evidence for multicomponent mantle  
841 metasomatism in the Ivrea Zone. *Earth and Planetary Science Letters* 310, 429-440.

- 842 Siena, F., Coltorti, M., 1989. The petrogenesis of a hydrated mafic - ultramafic complex and the  
843 role of amphibole fractionation at Finero (Italian Western Alps). *Neues Jahrbuch für Mineralogie* 6,  
844 255-274.
- 845 Sills, Jane D., Ackermann, D., Herd, Richard K., Windley, Brian F., 1983. Bulk composition and  
846 mineral parageneses of sapphirine-bearing rocks along a gabbro-lherzolite contact at Finero, Ivrea  
847 Zone, N Italy. *Journal of Metamorphic Geology* 1, 337-351.
- 848 Sinigoi, S., Quick, J. E., Mayer, A., Budhan, J., 1996. Influence of stretching and density contrasts  
849 on the chemical evolution of continental magmas: an example from the Ivrea-Verbano Zone.  
850 *Contributions to Mineralogy and Petrology* 123, 238-250.
- 851 Sinigoi, S., Quick, J. E., Demarchi, G., Klötzli, U., 2011. The role of crustal fertility in the  
852 generation of large silicic magmatic systems triggered by intrusion of mantle magma in the deep  
853 crust. *Contributions to Mineralogy and Petrology* 162, 691-707.
- 854 Smye, A.J., Stockli, D.F., 2014. Rutile U-Pb age depth profiling: a continuous record of  
855 lithospheric thermal evolution. *Earth and Planetary Science Letters* 408, 171-182.
- 856 Stähle, V., Frenzel, G., Kober, B., Michard, A., Puchelt, H., Schneider, W., 1990. Zircon syenite  
857 pegmatites in the Finero peridotite (Ivrea Zone): evidence for a syenite from a mantle source. *Earth  
858 and Planetary Science Letters* 101, 196-205.
- 859 Stähle, V., Frenzel, G., Hess, J. C., Saupé, F., Schmidt, S. Th., Schneider, W., 2001. Permian  
860 metabasalt and Triassic alkaline dykes in the Northern Ivrea Zone: clues to the post-Variscan  
861 geodynamic evolution of the Southern Alps. *Schweizerische Mineralogische und Petrographische  
862 Mitteilungen* 81, 1-21.
- 863 Steck, A., Tièche, J.C., 1976. Carte géologique de l'antiforme péridotitique de Finero avec des  
864 observations sur les phases de déformation et de recristallisation. *Bulletin Suisse de Minéralogie et  
865 de Pétrographie* 56, 501-512.
- 866 Tiepolo, M., 2003. Pb geochronology of zircon with laser ablation inductively coupled plasma-mass  
867 spectrometry. *Chemical Geology* 199, 159-177.

- 868 Tribuzio, R., Renna, M.R., Dallai, L., Zanetti, A., 2014. The magmatic–hydrothermal transition in  
869 the lower oceanic crust: Clues from the Ligurian ophiolites, Italy. *Geochimica et Cosmochimica*  
870 *Acta* 130, 188-211.
- 871 Tumati, S., Thöni M., Nimis P., Martin S., Mair V., 2003. Mantle-crust interactions during  
872 Variscan subduction in the Eastern Alps (Nonsberg-Ulten zone): geochronology and new  
873 petrological constraints. *Earth and Planetary Science Letters* 210, 509-526.
- 874 Van Achterbergh, E., Ryan, C.G., Jackson, S.E., Griffin, W.L., 2001. Data reduction software for  
875 LA-ICP-MS: appendix. In: Sylvester, P.J. (Ed.), *Laser Ablation-ICP-Mass Spectrometry in the*  
876 *Earth Sciences: Principles and Applications*, Mineralog. Assoc. Canada (MAC) Short Course  
877 Series, Ottawa, Ontario, Canada, 29, 239-243.
- 878 Vavra, G., Schmid, R. and Gebauer, D., 1999. Internal morphology, habit and U-Th-Pb  
879 microanalysis of amphibolite-to-granulite facies zircons: Geochronology of the Ivrea Zone  
880 (Southern Alps). *Contributions to Mineralogy and Petrology* 134, 380-404.
- 881 Vavra, G., Schaltegger, U., 1999. Post-granulite facies monazite growth and rejuvenation during  
882 Permian to Lower Jurassic thermal and fluid events in the Ivrea Zone (Southern Alps).  
883 *Contributions to Mineralogy and Petrology* 134, 405-414.
- 884 Vignola, P., Diella V., Oppizzi P., Tiepolo M., Weiss S., 2008. Phosphate assemblages from the  
885 Brissago granitic pegmatite, western Southern Alps, Switzerland. *The Canadian Mineralogist* 46,  
886 635-650.
- 887 von Quadt, A., Ferrario, A., Diella, V., Hansmann, W., Vavra, G., Köppel, V., 1993. U-Pb ages of  
888 zircons from chromitites of the phlogopite peridotite of Finero, Ivrea Zone, N-Italy. *Schweizerische*  
889 *Mineralogische und Petrographische Mitteilungen* 73, 137-138.
- 890 Voshage, H., Hunziker, J.C., Hofmann, A.W., Zingg, A., 1987. A Nd and Sr isotopic study of the  
891 Ivrea zone, Southern Alps, N-Italy. *Contributions to Mineralogy and Petrology* 97, 31-42.

- 892 Voshage, H., Sinigoi, S., Mazzucchelli, M., Demarchi, G., Rivalenti, G., Hofmann, A.W., 1988.  
893 Isotopic constraints on the origin of ultramafic and mafic dikes in the Balmuccia peridotite  
894 (Ivrea Zone). *Contributions to Mineralogy and Petrology* 100(3), 261-267.
- 895 Wiedenbeck, M., Alle, P., Corfu, F., Griffin, W.L., Meier, M., Oberli, F., von Quadt, A., Roddick,  
896 J.C., Spiegel, W., 1995. Three natural zircon standards for U–Th–Pb, Lu–Hf, trace elements and  
897 REE analyses. *Geostandard Newsletter* 19, 1-23.
- 898 Woodhead, J.D., Hergt, J.M., 2005. A preliminary appraisal of seven natural zircon reference  
899 materials for in-situ Hf-isotope analysis. *Geostandard and Geoanalytical Research* 29, 183–195.
- 900 Wolff, R., Dunkl, I., Kiesselbach, G., Wemmer, K., Siegesmund S., 2012. Zircon (U–Th)/He and  
901 fission track constraints on the exhumation history of the Ivrea-Verbano Zone of the Southern Alps.  
902 *Tectonophysics* 579, 104-117.
- 903 Wu, F.Y., Yang, Y.H., Xie, L.W., Yang, J.H., Xu, P., 2006. Hf isotopic compositions of the  
904 standard zircons and baddeleyites used in U–Pb geochronology. *Chemical Geology* 234, 105-126.
- 905 Wu, F.-Y., Yang, J.-H., Wilde, S.A., Liu, M.-X., Guo, J.-H., Zhai, M.-G., 2007. Detrital zircon U–  
906 Pb and Hf isotopic constrains on the crustal evolution of North Korea. *Precambrian Research* 159,  
907 155–177.
- 908 Zaccarini, F., Stumpfl, E.F., Garuti, G., 2004. Zirconolite and Zr–Th–U minerals in chromitites of  
909 the Finero complex, western Alps, Italy: evidence for carbonatite-type metasomatism in a  
910 subcontinental mantle plume. *The Canadian Mineralogist* 42, 1825-1845.
- 911 Zanetti, A., Mazzucchelli, M., Rivalenti, G., Vannucci, R., 1999. The Finero phlogopite-peridotite  
912 massif: an example of subduction-related metasomatism. *Contributions to Mineralogy and*  
913 *Petrology* 134, 107-122.
- 914 Zanetti, A., Mazzucchelli, M., Sinigoi, S., Giovanardi, T., Peressini, G., Fanning, M., 2013.  
915 SHRIMP U–Pb Zircon Triassic Intrusion Age of the Finero Mafic Complex (Ivrea-Verbano Zone,  
916 Western Alps) and its Geodynamic Implications. *Journal of Petrology* 54, 2225-2265.

- 917 Zanetti, A., Mazzucchelli, M., Sinigoi, S., Giovanardi, T., Peressini, G., Fanning, M., 2014.  
918 SHRIMP U-Pb Zircon Triassic Intrusion Age of the Finero Mafic Complex (Ivrea-Verbano Zone,  
919 Western Alps) and its Geodynamic Implications. *Journal of Petrology* 55(6), 1239-1240.
- 920 Zingg, A., Handy, M. R., Hunziker, J. C., Schmid, S.M., 1990. Tectonometamorphic history of the  
921 Ivrea Zone and its relationship to the crustal evolution of the Southern Alps. *Tectonophysics* 182,  
922 169-192.
- 923 Zhou, M.F., Robinson, P.T., Bai, W.J., 1994. Formation of podiform chromitites by melt/rock  
924 interaction in the upper mantle. *Mineralium Deposita* 29(1), 98-101.
- 925 Zhou, M.-Fu, Robinson, P.T., Malpas, J., Li, Z., 1996. Podiform Chromitites in the Luobusa  
926 Ophiolite (Southern Tibet): Implications for Melt-Rock Interaction and Chromite Segregation in the  
927 Upper Mantle. *Journal of Petrology* 37(1), 3-21.

928

929 **Figure Captions**

930 Figure 1 – (a) Sketch map of the Ivrea-Verbano Zone, which represents the westernmost part of the  
931 Southern Alps. The rectangle indicates the location of the map of the Finero Complex in (b). CL,  
932 Cremosina Line; IL, Insubric Line; CMBL, Cossato-Mergozzo-Brissago Line; PL, Pogallo Line;  
933 HTSZ, high-temperature shear zone of the Anzola-Val Grande area (Brodie and Rutter, 1987;  
934 Rivalenti and Mazzucchelli, 2000; Rutter et al., 2007). (b) Sketch map of the Finero Complex  
935 modified after Steck and Tièche (1976). The empty stars document the locations of the zircon-  
936 bearing chromitites here studied.

937

938 Figure 2 – (a) The thickest layer of the FI09C34 chromitite swarm; (b) Chromitite pocket in sample  
939 FI09C34; (c) Texture of MR01CR chromitite, which is characterised by segregation of anhedral  
940 large chromite overgrowing a matrix formed by porphyroclastic dunite; (d) Allotriomorphic texture  
941 of chromite FI09C04 formed by chromite and orthopyroxene, where rounded olivine relicts rarely

942 occur within large orthopyroxene; (e) Allotriomorphic texture of chromitite FI09C34, with presence  
943 of serpentinisation along the grain boundary.

944

945 Figure 3 – Cathodoluminescence images of zircons from FI09C04, FI09C34 and MR01CR.

946 FI09C04 and FI09C34 zircons are virtually free from internal structures, while some of those from  
947 MR01CR show broad darker areas, usually returning relatively older ages than the lighter ones.

948 Spot analyses are reported together with single-spot concordant ages.

949

950 Figure 4 - Age histogram and relative probability diagram of chromitite zircons of this study.

951 Maximum probability age is reported for each sample.

952

953 Figure 5 - Concordia ages calculated with  $^{206}\text{Pb}/^{238}\text{U}$  and  $^{207}\text{Pb}/^{235}\text{U}$  ratios for chromitite zircons  
954 from MR01CR, FI09C34 and FI09C04 samples.

955

956 Figure 6 – Major element mineral chemistry of chromitites of this study. Data from literature are  
957 reported for comparison: FPP harzburgite-pyroxenite association (Harz-Py) from Zanetti et al.  
958 (1999) (a) and Grieco et al. (2001) (c); average FPP harzburgite (Avg. Harz) from Siena and  
959 Coltorti (189) (b); chromitite veins (Chromitite) from Grieco et al. (2001, 2004) (c, d)..

960

961 Figure 7 – (a) CI-normalised (Lyubetskaya and Korenaga, 2007) REE patterns and (b) Pyrolite-  
962 normalised (McDonough and Sun, 1995) extended trace element diagrams of clinopyroxenes from  
963 FI09C04 and FI09C34 chromitites. Literature data are reported for comparison: amphibole from  
964 apatite-bearing wehrlites (Ap-Wehrl Amph) and its host harzburgite (Harz Ap-free Amph) from  
965 Morishita et al. (2008) (a); clinopyroxene from the harzburgite-pyroxenite association (Harz-Py  
966 Cpx) and apatite-bearing wehrlite (Ap-Wehrl Cpx) from Zanetti et al. (1999) (b); clinopyroxene  
967 from harzburgite (Harz Cpx) and chromitite veins (Chromitite Cpx) from Grieco et al. (2001) (c).

968

969 Figure 8 – (a) CI-normalised (Lyubetskaya and Korenaga, 2007) REE patterns and (b) Pyrolite-  
970 normalised (McDonough and Sun, 1995) extended trace element diagrams for zircons from the  
971 chromitites of this study. Data from zircons from (a) gabbros of the EG (Zanetti et al., 2013) and (b)  
972 from alkaline dykes within the Mafic Complex (Schaltegger et al., 2015) are reported for  
973 comparison.

974

975 Figure 9 –  $\epsilon\text{Hf}(t)$  vs U-Pb age for the zircons from the chromitites of this study. Literature data of  
976 (a) zircons from miaskite-type nepheline pegmatites in the Finero Mafic Complex (Schaltegger et  
977 al., 2015) and (b) FPP chromitites (Badanina et al., 2013). The Depleted Mantle (DM) evolution  
978 line is calculated using the values of present-day  $^{176}\text{Hf}/^{177}\text{Hf}$  ratio of 0.28325 from Nowell et al.,  
979 1998, and  $^{176}\text{Lu}/^{177}\text{Hf}$  ratio of 0.0384 from Griffin et al., 2000). CHUR values are from Blichert-  
980 Toft and Albarede (1997).

981

982 Figure 10 – Isotopic oxygen composition ( $\delta^{18}\text{O}$  mineral vs. SMOW‰) of orthopyroxene (Opx) and  
983 clinopyroxene (Cpx) separates from FI09C04 and FI09C34 chromitites, and of orthopyroxene and  
984 zircon (Zrc) separates from MR01CR. FPP data for minerals (Ol = olivine; Cpx = clinopyroxene;  
985 Amph = amphibole; Phl = phlogopite) of the harzburgite-pyroxenite association (Harz-Py) from  
986 Hartmann and Wedephol (1993) (a) and Selverstone and Sharp (2011) (b) are reported for  
987 comparison, as well as the range of mantle peridotites and mantle-derived melts from Bindeman  
988 (2008) (\*) and zircon values from a hornblende-gabbro and a hornblendite from the Ligurian  
989 ophiolites (Tribuzio et al., 2014) (c).

990

### 991 **Table Captions**

992 Table 1: summary of ELA-ICP-HRMS U-Pb zircon analysis from chromitite layers from FPP.

993

994 Table 2: summary of MC-ICP-MS *in-situ* Hf isotopic compositions of zircon from FPP.

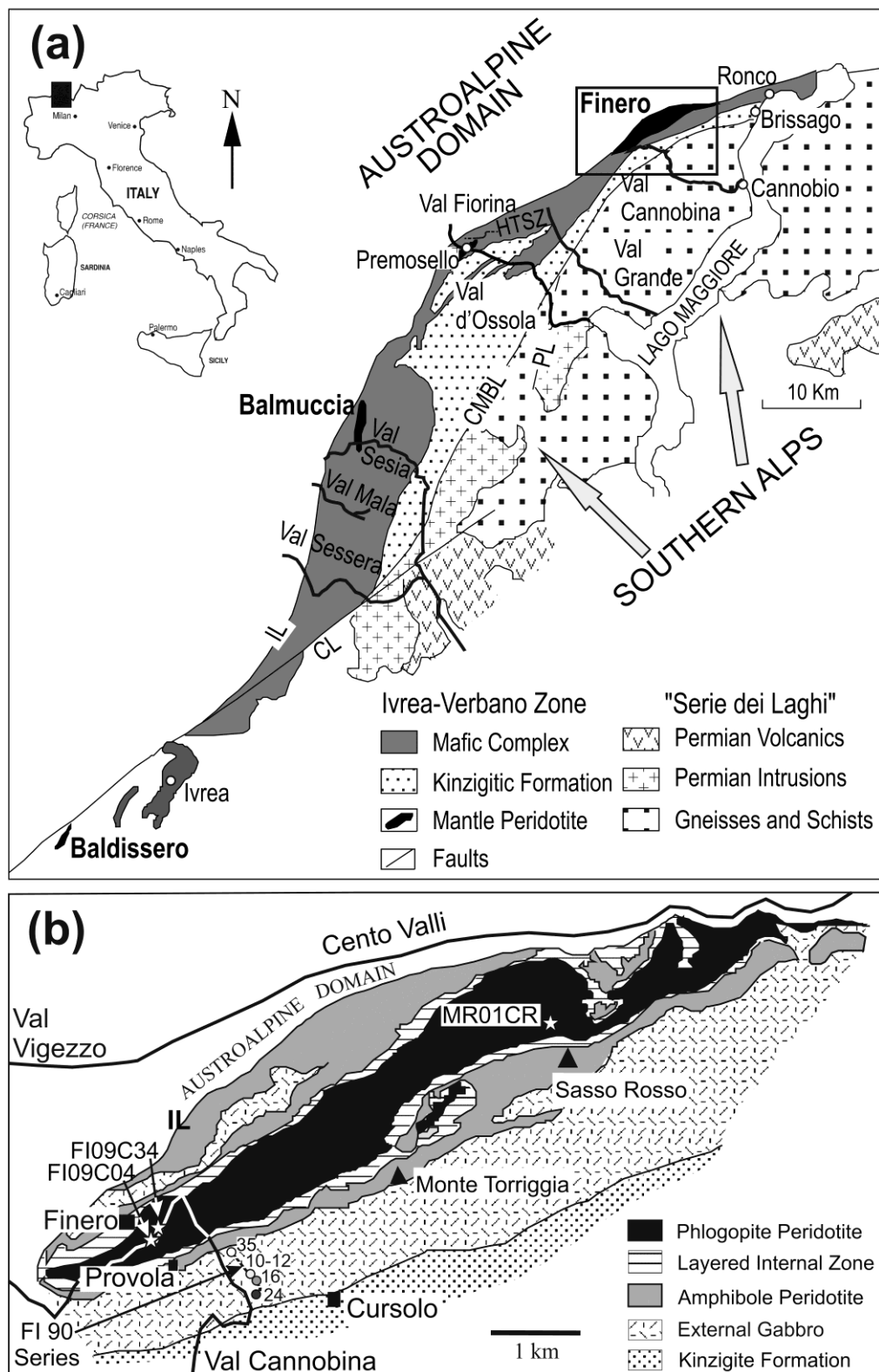
995

996 Table 3: Isotopic oxygen composition ( $\delta^{18}\text{O}$  vs. SMOW‰) of mineral separates from the FPP  
997 chromitites here studied . Numbers between parenthesis represent the number of replicates of the  
998 measurements on different aliquots of the same sample.

999

ACCEPTED MANUSCRIPT

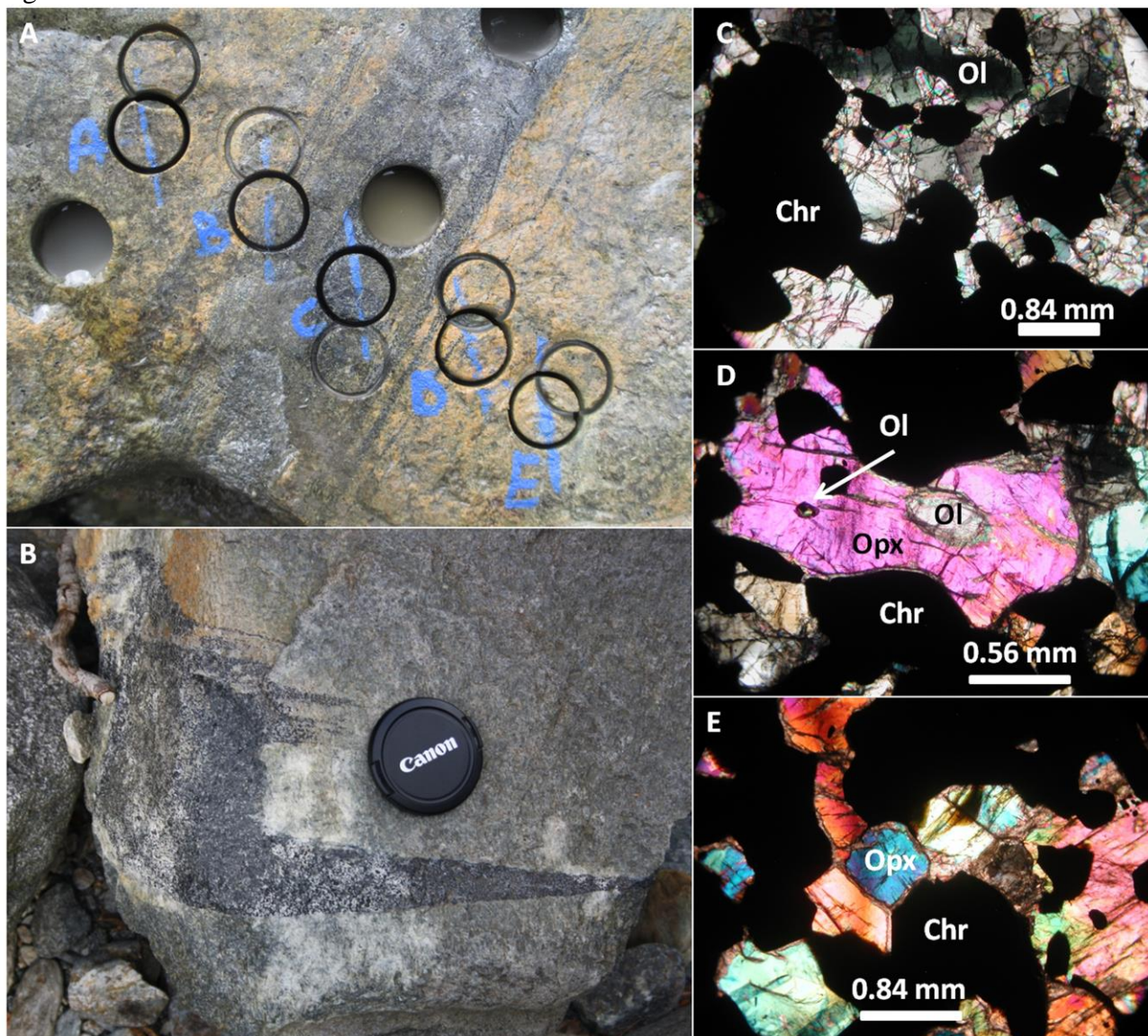
1000 Fig. 1



1001

1002

1003 Fig. 2

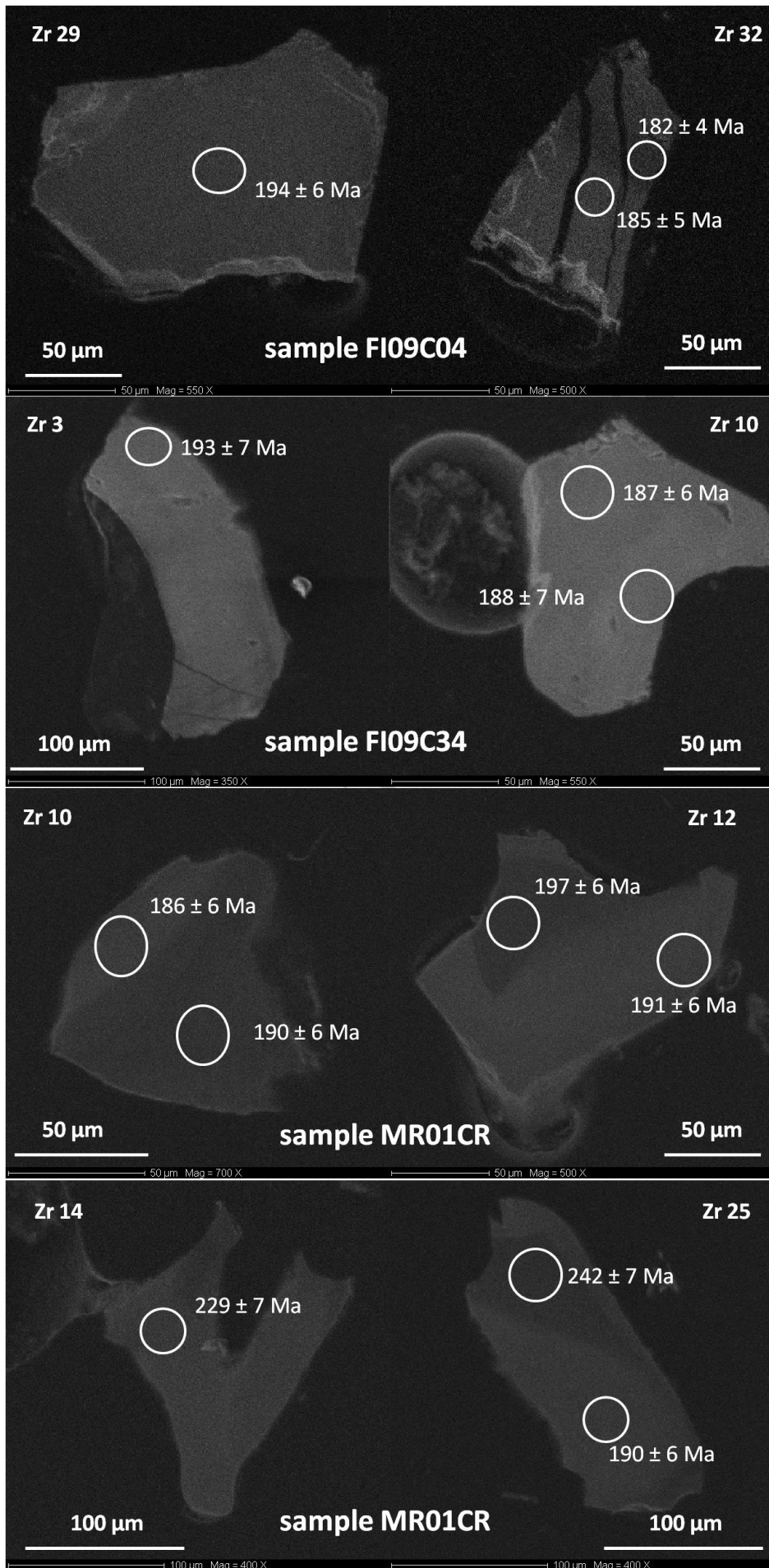


1004

1005

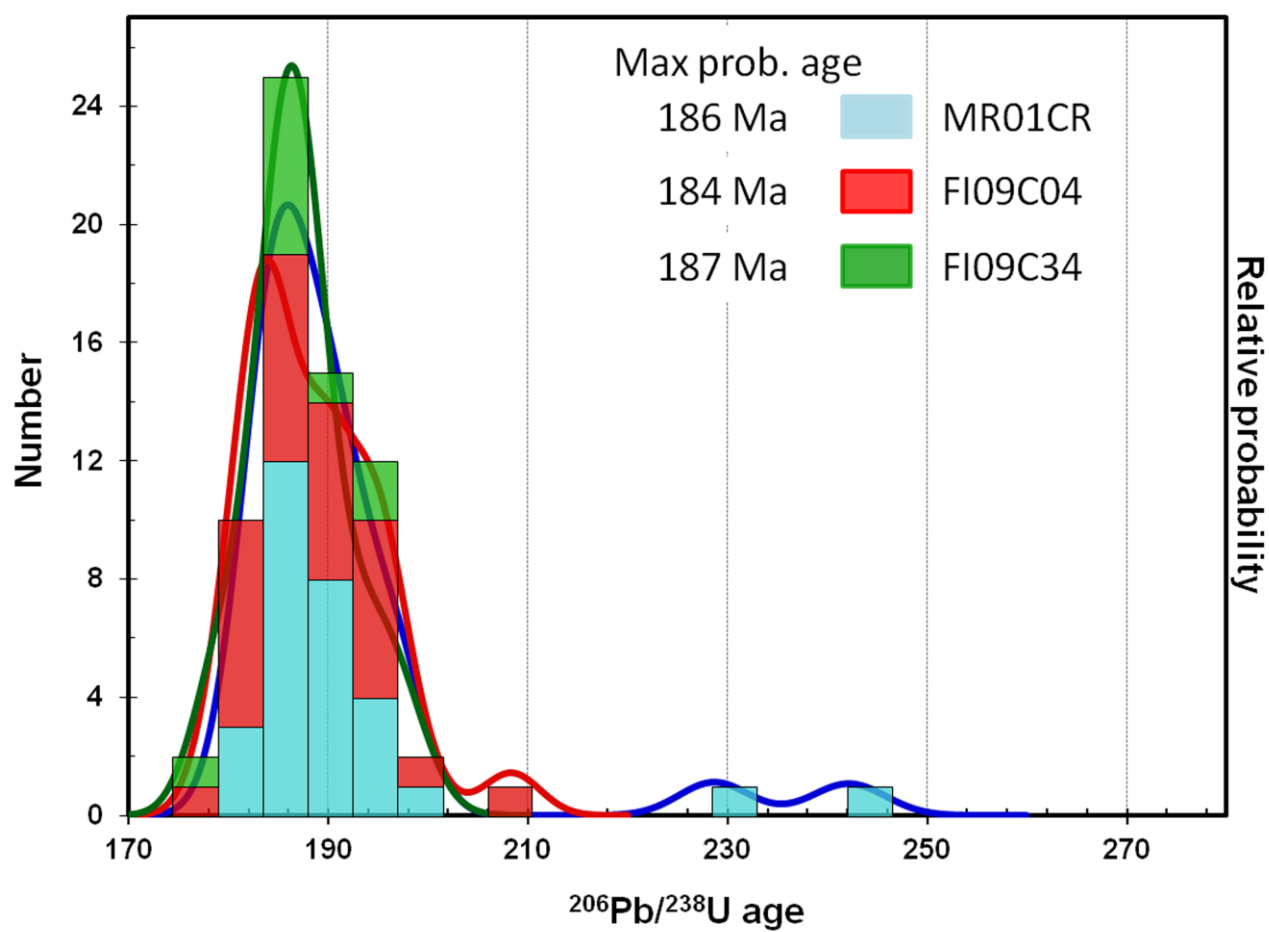
1006 Fig. 3

ACCEPTED MANUSCRIPT



ACCEPTED MANUSCRIPT

1009 Fig. 4

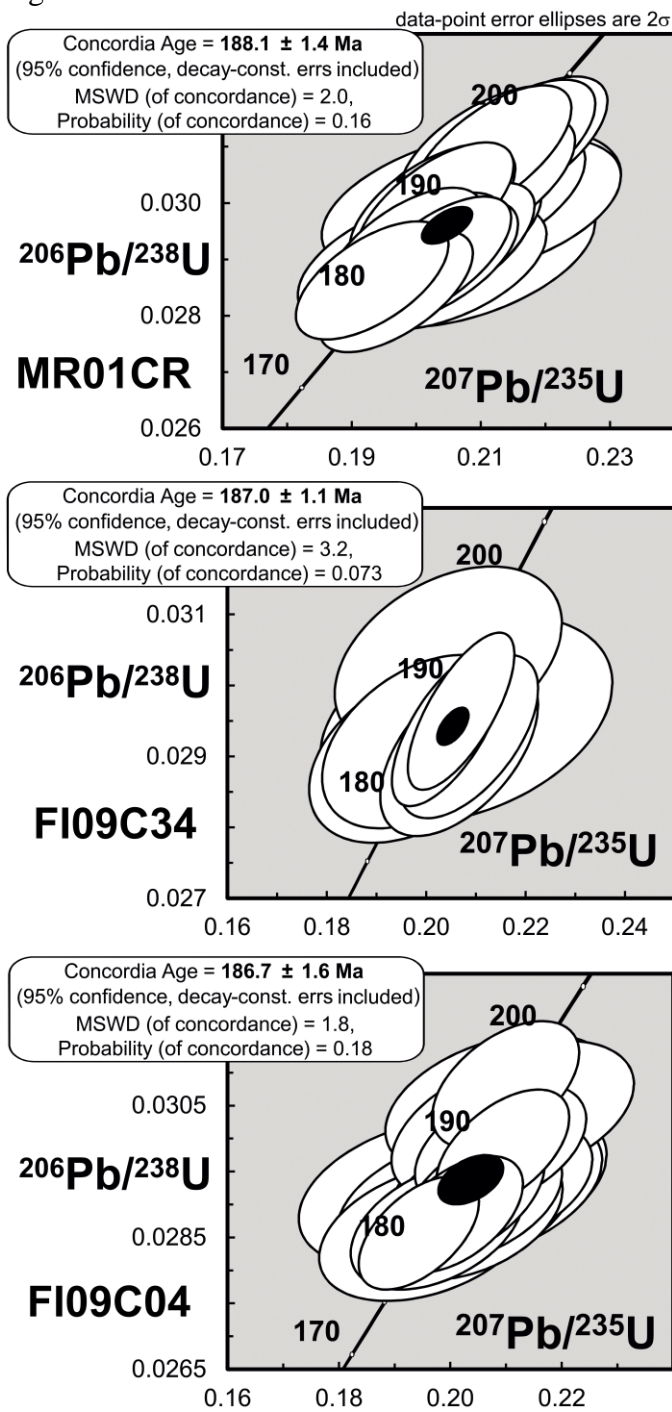


1010

1011

ACCEPTED

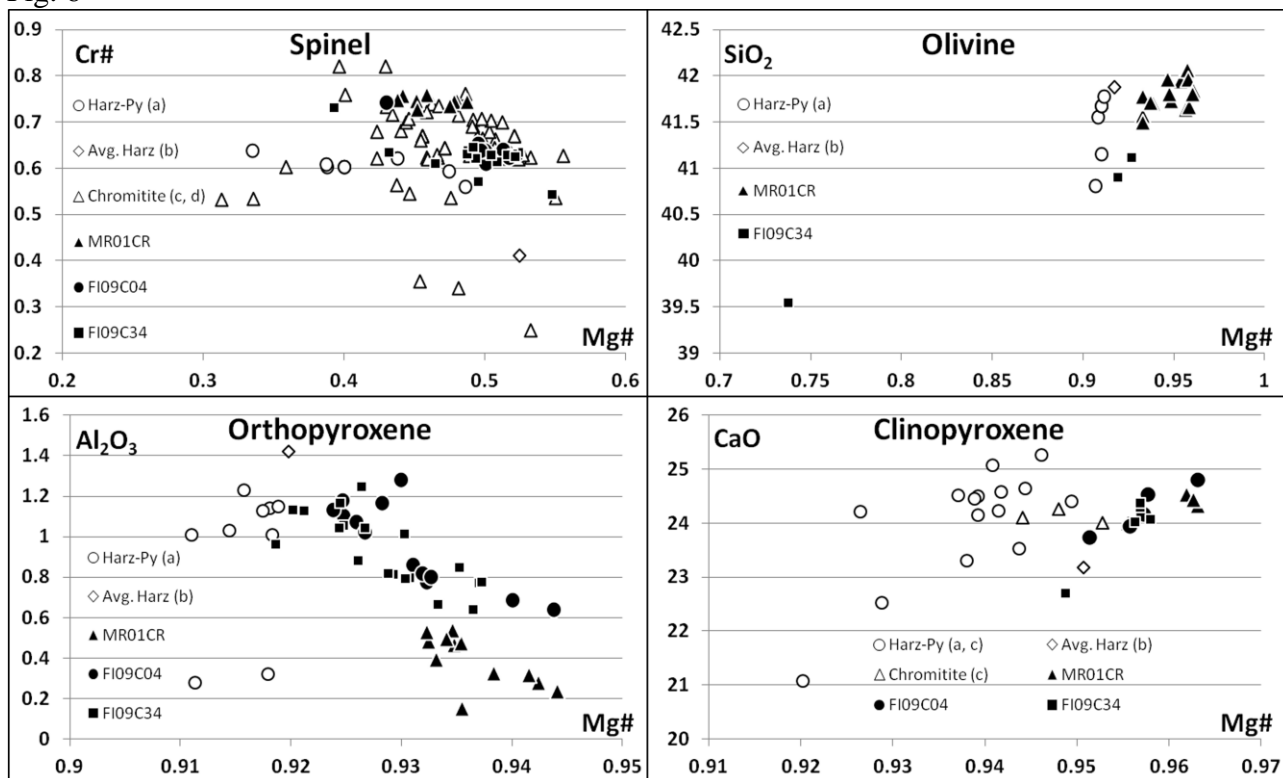
1012 Fig. 5



1013

1014

1015 Fig. 6

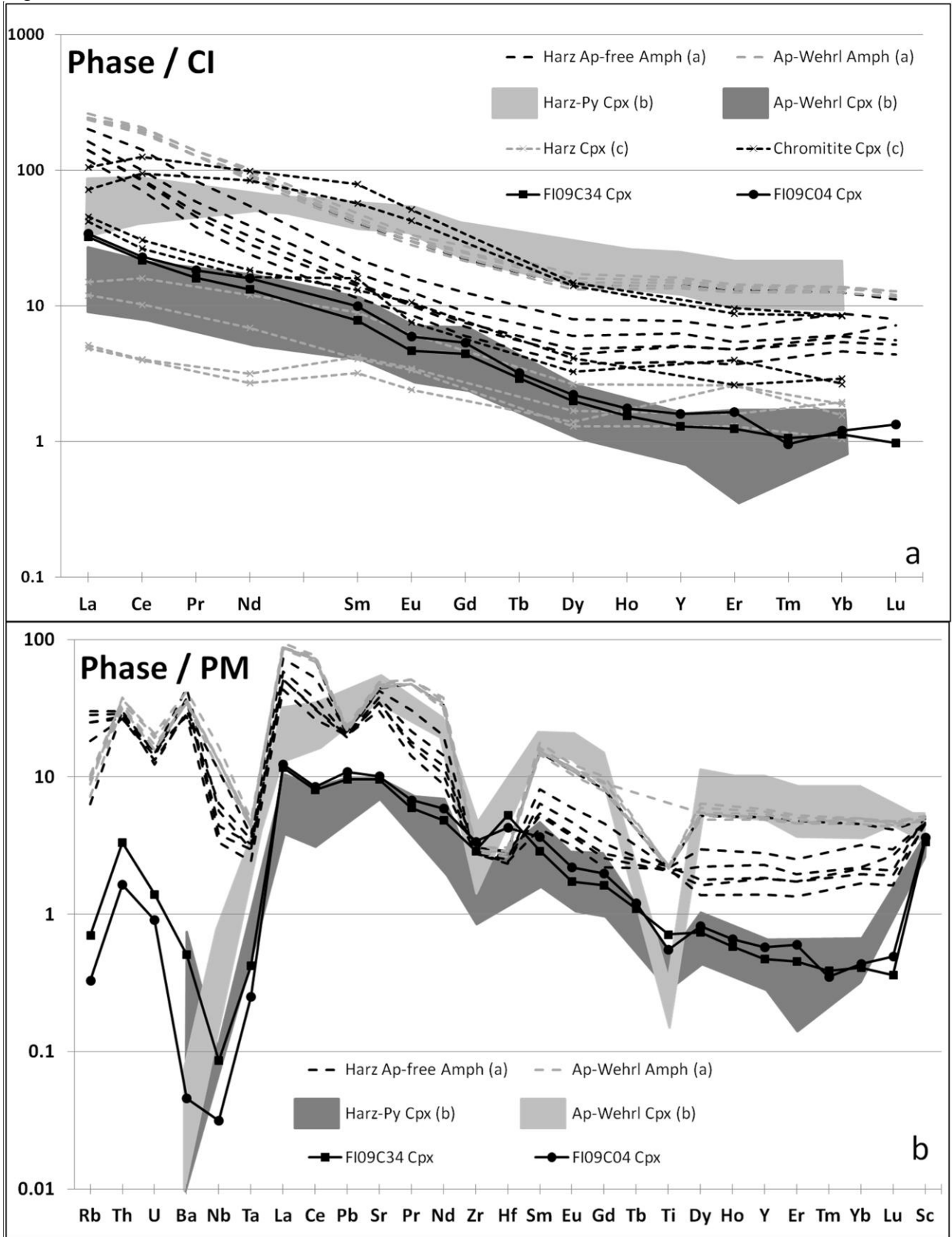


1016

1017

ACCEPTED

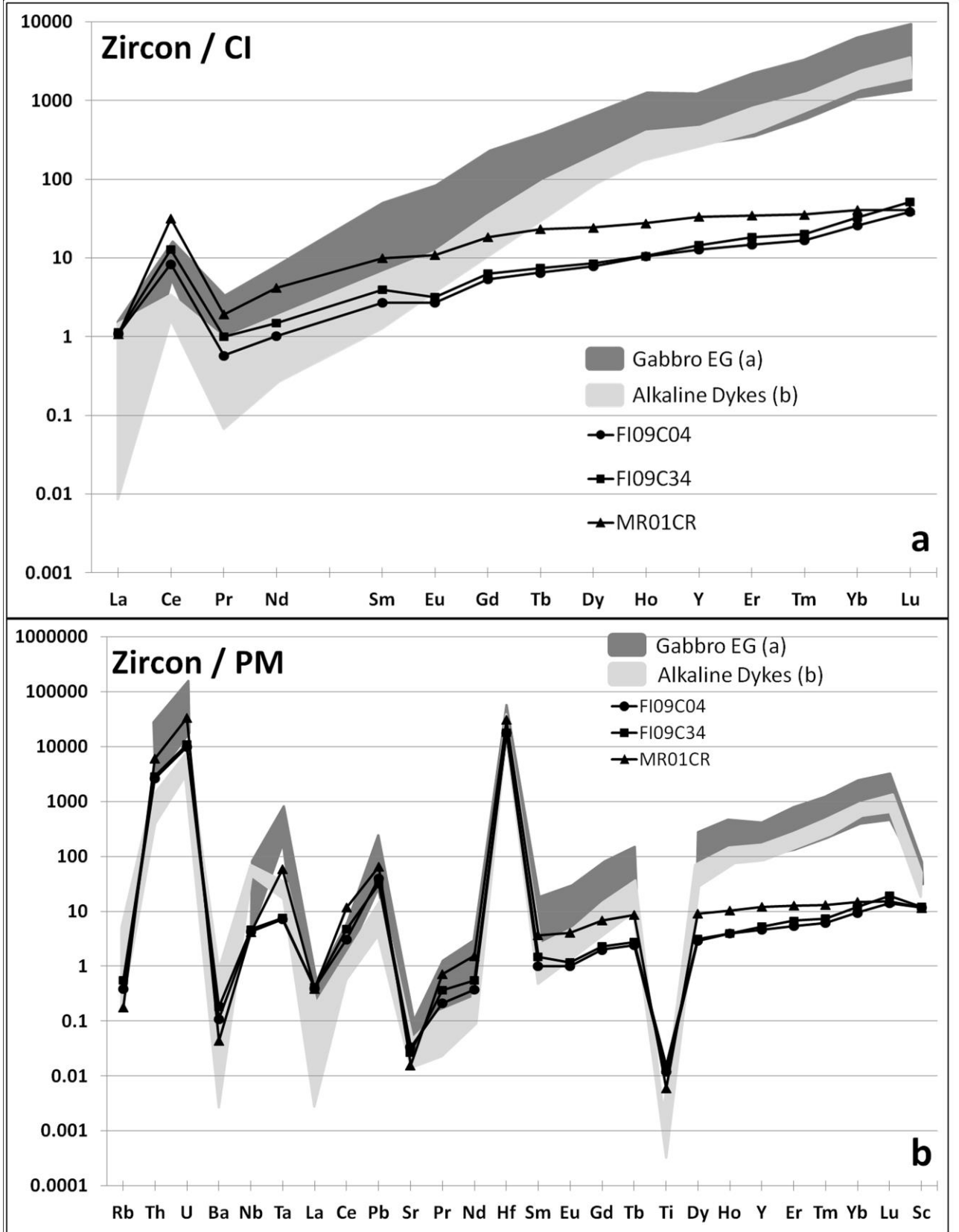
1018 Fig. 7



1019

1020

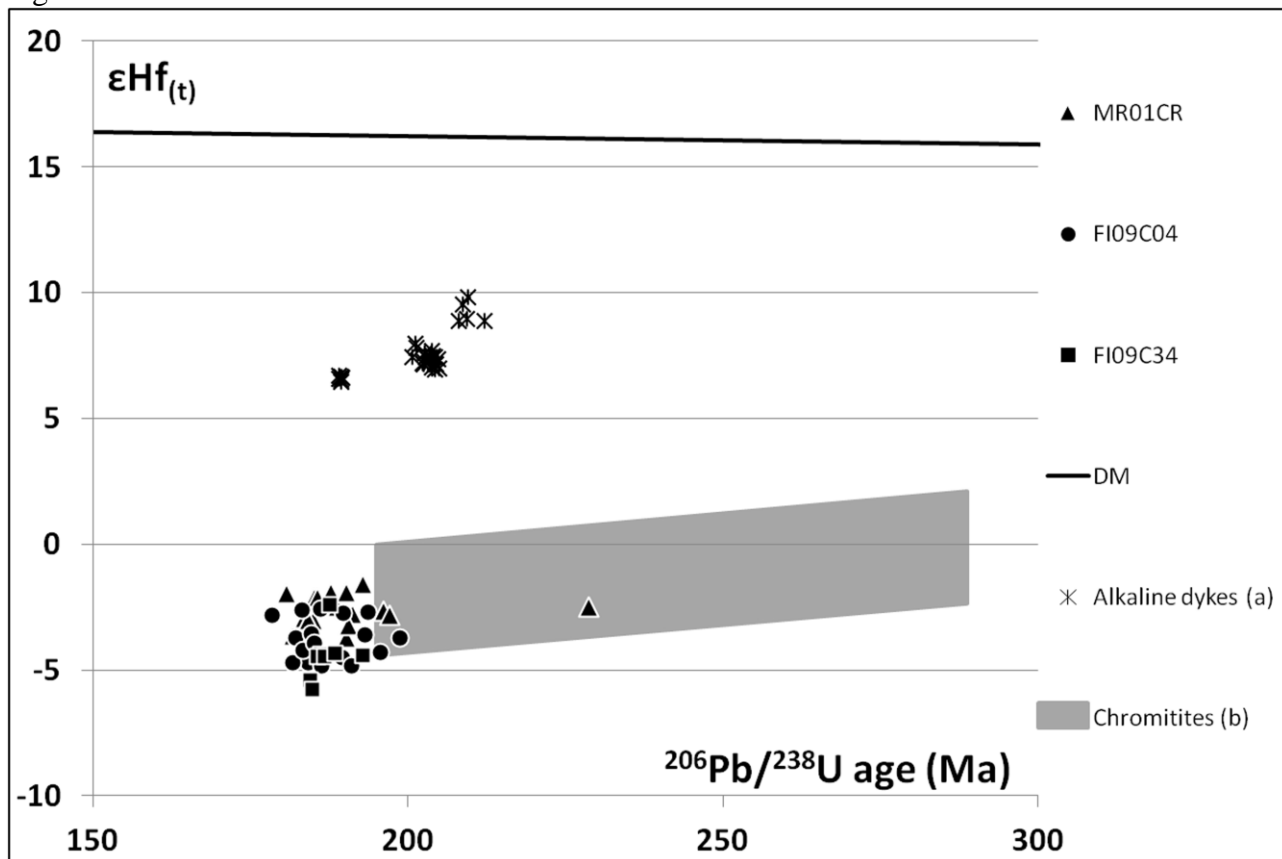
1021 Fig. 8



1022

1023

1024 Fig. 9

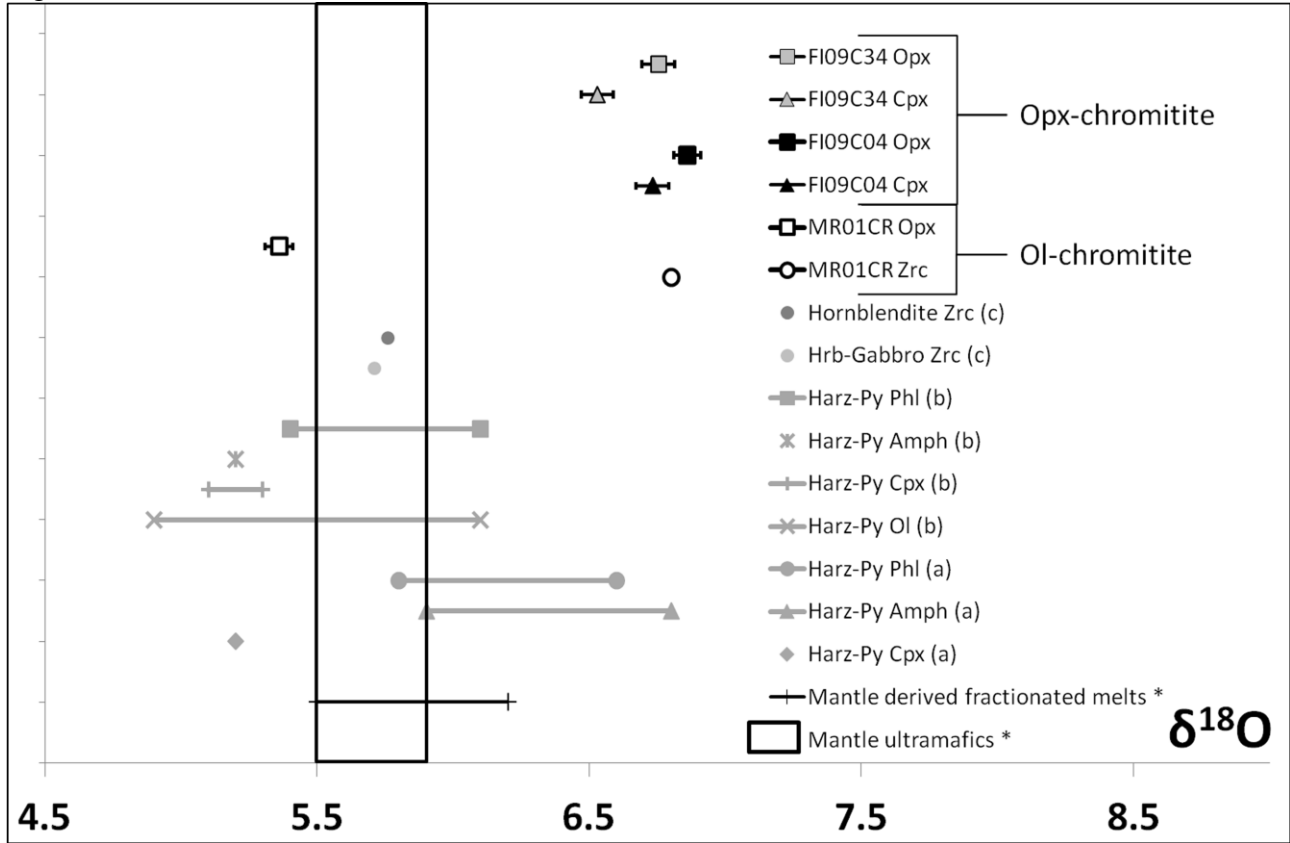


1025

1026

ACCEPTED

1027 Fig. 10



1030  
1031

Table 1: summary of ELA-ICP-HRMS U-Pb zircon analysis from chromitite layers from FPP.

| Samp<br>le:<br>Zirco<br>n | MR01<br>CR<br>Positi<br>on | $^{207}\text{Pb}/^{206}\text{Pb}$ |            | Ratio<br>$^{206}\text{Pb}/^{238}\text{U}$ |            | $^{207}\text{Pb}/^{235}\text{U}$ |            | $^{207}\text{Pb}/^{206}\text{Pb}$ |            | Ages<br>$^{206}\text{Pb}/^{238}\text{U}$ |    | $^{207}\text{Pb}/^{235}\text{U}$ |     | Concor<br>dia | 2<br>$\sigma$ | % of<br>discordance |
|---------------------------|----------------------------|-----------------------------------|------------|---|------------|----------------------------------|------------|-----------------------------------|------------|--|----|----------------------------------|-----|---------------|---------------|---------------------|
|                           |                            | 1 $\sigma$                        | 1 $\sigma$ | 1 $\sigma$                                | 1 $\sigma$ | 2 $\sigma$                       | 2 $\sigma$ | 2 $\sigma$                        | 2 $\sigma$ |  |    |                                  |     |               |               |                     |
| 7                         | core                       | 0.0498                            | 0.00       | 0.0292                                    | 0.00       | 0.2005                           | 0.00       | 187.1                             | 8.3        | 185.4                                    | 9  | 185.6                            | 9.1 |               |               |                     |
|                           |                            |                                   | 11         |   | 0.00       |                                  | 0.00       |                                   |            |  | 6. |                                  |     |               | 6.            |                     |
| 9                         | core                       | 0.0497                            | 0.00       | 0.0309                                    | 0.00       | 0.2115                           | 0.00       | 178.6                             | 7.8        | 196.2                                    | 2  | 194.8                            | 9.4 | 196.1         | 1             | 0.69%               |
|                           |                            |                                   | 11         |   | 0.00       |                                  | 0.00       |                                   |            |  | 5. |                                  |     |               | 5.            |                     |
| 9                         | rim                        | 0.0507                            | 0.00       | 0.0290                                    | 0.00       | 0.2027                           | 0.00       | 227.7                             | 9.9        | 184.3                                    | 8  | 187.4                            | 9.0 | 184.4         | 7             | -1.70%              |
|                           |                            |                                   | 11         |   | 0.00       |                                  | 0.00       |                                   |            |  | 6. |                                  |     |               | 5.            |                     |
| 10                        | core                       | 0.0492                            | 0.00       | 0.0299                                    | 0.00       | 0.2029                           | 0.00       | 157.4                             | 7.0        | 190.0                                    | 0  | 187.6                            | 9.2 | 189.9         | 9             | 1.31%               |
|                           |                            |                                   | 11         |   | 0.00       |                                  | 0.00       |                                   | 11.        |  | 5. |                                  |     |               | 5.            |                     |
| 10                        | rim                        | 0.0511                            | 0.00       | 0.0292                                    | 0.00       | 0.2057                           | 0.00       | 244.0                             | 2          | 185.7                                    | 9  | 189.9                            | 9.5 | 185.8         | 8             | -2.29%              |
|                           |                            |                                   | 12         |   | 0.00       |                                  | 0.00       |                                   |            |  | 6. |                                  |     |               | 6.            |                     |
| 12                        | core                       | 0.0503                            | 0.00       | 0.0310                                    | 0.00       | 0.2148                           | 0.00       | 209.8                             | 9.5        | 196.9                                    | 1  | 197.5                            | 9.7 | 196.9         | 0             | -0.34%              |
|                           |                            |                                   | 11         |   | 0.00       |                                  | 0.00       |                                   | 13.        |  | 6. |                                  | 11. |               | 6.            |                     |
| 12                        | rim                        | 0.0511                            | 0.00       | 0.0301                                    | 0.00       | 0.2111                           | 0.00       | 245.3                             | 5          | 191.2                                    | 2  | 194.4                            | 4   | 191.3         | 1             | -1.68%              |
|                           |                            |                                   | 14         |   | 0.00       |                                  | 0.00       |                                   | 10.        |  | 7. |                                  | 11. |               | 7.            |                     |
| 14                        | core                       | 0.0509                            | 0.00       | 0.0361                                    | 0.00       | 0.2531                           | 0.00       | 238.1                             | 8          | 228.7                                    | 1  | 229.1                            | 2   | 228.7         | 0             | -0.19%              |
|                           |                            |                                   | 12         |   | 0.00       |                                  | 0.00       |                                   |            |  | 5. |                                  |     |               | 5.            |                     |
| 16                        | core                       | 0.0494                            | 0.00       | 0.0292                                    | 0.00       | 0.1981                           | 0.00       | 165.0                             | 7.6        | 185.3                                    | 8  | 183.5                            | 9.2 | 185.2         | 7             | 0.95%               |
|                           |                            |                                   | 11         |   | 0.00       |                                  | 0.00       |                                   | 20.        |  | 6. |                                  | 14. |               | 6.            |                     |
| 16                        | rim                        | 0.0516                            | 0.00       | 0.0291                                    | 0.00       | 0.2079                           | 0.00       | 269.1                             | 4          | 184.8                                    | 6  | 191.8                            | 9   | 184.9         | 5             | -3.80%              |
|                           |                            |                                   | 20         |   | 0.00       |                                  | 0.00       |                                   | 10.        |  | 6. |                                  |     |               | 6.            |                     |
| 17                        | core                       | 0.0506                            | 0.00       | 0.0311                                    | 0.00       | 0.2163                           | 0.00       | 222.2                             | 2          | 197.1                                    | 2  | 198.9                            | 9.9 | 197.2         | 1             | -0.88%              |
|                           |                            |                                   | 12         |   | 0.00       |                                  | 0.00       |                                   |            |  | 6. |                                  | 10. |               | 6.            |                     |
| 18                        | core                       | 0.0498                            | 0.00       | 0.0309                                    | 0.00       | 0.2116                           | 0.00       | 186.1                             | 9.6        | 196.2                                    | 2  | 194.9                            | 7   | 196.1         | 1             | 0.67%               |
|                           |                            |                                   | 13         |   | 0.00       |                                  | 0.00       |                                   | 10.        |  | 6. |                                  |     |               | 6.            |                     |
| 20                        | core                       | 0.0506                            | 0.00       | 0.0304                                    | 0.00       | 0.2118                           | 0.00       | 224.0                             | 0          | 192.8                                    | 1  | 195.1                            | 9.6 | 192.9         | 0             | -1.17%              |
|                           |                            |                                   | 11         |   | 0.00       |                                  | 0.00       |                                   |            |  | 5. |                                  |     |               | 5.            |                     |
| 21                        | core                       | 0.0492                            | 0.00       | 0.0299                                    | 0.00       | 0.2025                           | 0.00       | 157.8                             | 7.6        | 190.0                                    | 9  | 187.2                            | 9.7 | 189.9         | 8             | 1.48%               |
|                           |                            |                                   | 12         |   | 0.00       |                                  | 0.00       |                                   | 13.        |  | 6. |                                  | 11. |               | 5.            |                     |
| 23                        | core                       | 0.0506                            | 0.00       | 0.0291                                    | 0.00       | 0.2018                           | 0.00       | 224.0                             | 2          | 185.0                                    | 0  | 186.7                            | 5   | 185.1         | 9             | -0.88%              |
|                           |                            |                                   | 15         |   | 0.00       |                                  | 0.00       |                                   | 10.        |  | 6. |                                  | 10. |               | 6.            |                     |
| 24                        | core                       | 0.0502                            | 0.00       | 0.0297                                    | 0.00       | 0.2054                           | 0.00       | 204.3                             | 0          | 188.7                                    | 1  | 189.7                            | 0   | 188.7         | 0             | -0.56%              |
|                           |                            |                                   | 12         |   | 0.00       |                                  | 0.00       |                                   | 11.        |  | 7. |                                  | 11. |               | 7.            |                     |
| 25                        | core                       | 0.0513                            | 0.00       | 0.0383                                    | 0.00       | 0.2697                           | 0.00       | 253.0                             | 3          | 242.2                                    | 4  | 242.4                            | 8   | 242.2         | 3             | -0.11%              |
|                           |                            |                                   | 11         |   | 0.00       |                                  | 0.00       |                                   | 20.        |  | 6. |                                  | 14. |               | 6.            |                     |
| 25                        | rim                        | 0.0519                            | 0.00       | 0.0299                                    | 0.00       | 0.2125                           | 0.00       | 282.3                             | 4          | 190.1                                    | 3  | 195.7                            | 4   | 190.2         | 3             | -2.92%              |
|                           |                            |                                   | 19         |   | 0.00       |                                  | 0.00       |                                   |            |  | 5. |                                  |     |               | 5.            |                     |
| 26                        | core                       | 0.0491                            | 0.00       | 0.0286                                    | 0.00       | 0.1931                           | 0.00       | 150.7                             | 7.0        | 182.0                                    | 5  | 179.3                            | 8.9 | 181.8         | 4             | 1.48%               |
|                           |                            |                                   | 11         |   | 0.00       |                                  | 0.00       |                                   | 12.        |  | 5. |                                  | 10. |               | 5.            |                     |
| 27                        | core                       | 0.0507                            | 0.00       | 0.0292                                    | 0.00       | 0.2038                           | 0.00       | 227.7                             | 2          | 185.7                                    | 8  | 188.3                            | 6   | 185.7         | 7             | -1.43%              |
|                           |                            |                                   | 14         |   | 0.00       |                                  | 0.00       |                                   | 11.        |  | 5. |                                  | 10. |               | 5.            |                     |
| 28                        | core                       | 0.0507                            | 0.00       | 0.0295                                    | 0.00       | 0.2055                           | 0.00       | 225.8                             | 1          | 187.7                                    | 9  | 189.8                            | 0   | 187.8         | 8             | -1.14%              |
|                           |                            |                                   | 12         |   | 0.00       |                                  | 0.00       |                                   | 12.        |  | 6. |                                  | 10. |               | 5.            |                     |
| 28                        | rim                        | 0.0508                            | 0.00       | 0.0295                                    | 0.00       | 0.2055                           | 0.00       | 232.2                             | 1          | 187.2                                    | 0  | 189.7                            | 5   | 187.3         | 9             | -1.37%              |
|                           |                            |                                   | 13         |   | 0.00       |                                  | 0.00       |                                   |            |  | 5. |                                  |     |               | 5.            |                     |
| 30                        | core                       | 0.0504                            | 0.00       | 0.0284                                    | 0.00       | 0.1968                           | 0.00       | 212.1                             | 9.7        | 180.7                                    | 6  | 182.4                            | 9.0 | 180.8         | 5             | -0.95%              |
|                           |                            |                                   | 11         |   | 0.00       |                                  | 0.00       |                                   | 12.        |  | 6. |                                  | 12. |               | 5.            |                     |
| 30                        | rim                        | 0.0499                            | 0.00       | 0.0289                                    | 0.00       | 0.1977                           | 0.00       | 188.9                             | 1          | 183.8                                    | 0  | 183.1                            | 1   | 183.8         | 9             | 0.38%               |
|                           |                            |                                   | 16         |   | 0.00       |                                  | 0.00       |                                   | 19.        |  | 7. |                                  | 17. |               | 6.            |                     |
| 33                        | core                       | 0.0504                            | 0.00       | 0.0300                                    | 0.00       | 0.2085                           | 0.00       | 211.6                             | 1          | 190.4                                    | 0  | 192.3                            | 4   | 190.5         | 9             | -0.98%              |
|                           |                            |                                   | 23         |   | 0.00       |                                  | 0.00       |                                   |            |  | 5. |                                  |     |               | 5.            |                     |
| 34                        | core                       | 0.0502                            | 0.00       | 0.0291                                    | 0.00       | 0.2012                           | 0.00       | 204.3                             | 9.6        | 184.9                                    | 7  | 186.1                            | 9.4 | 185.0         | 6             | -0.64%              |
|                           |                            |                                   | 12         |   | 0.00       |                                  | 0.00       |                                   |            |  | 6. |                                  | 10. |               | 6.            |                     |
| 35                        | core                       | 0.0495                            | 0.00       | 0.0300                                    | 0.00       | 0.2048                           | 0.00       | 173.5                             | 9.1        | 190.4                                    | 2  | 189.2                            | 5   | 190.3         | 1             | 0.61%               |
|                           |                            |                                   | 13         |   | 0.00       |                                  | 0.00       |                                   | 10.        |  | 6. |                                  | 11. |               | 6.            |                     |
| 35                        | rim                        | 0.0497                            | 0.00       | 0.0301                                    | 0.00       | 0.2071                           | 0.00       | 182.4                             | 4          | 191.4                                    | 2  | 191.1                            | 4   | 191.4         | 1             | 0.14%               |
|                           |                            |                                   | 14         |   | 0.00       |                                  | 0.00       |                                   | 15.        |  | 5. |                                  | 11. |               | 5.            |                     |
| 38                        | core                       | 0.0516                            | 0.00       | 0.0289                                    | 0.00       | 0.2047                           | 0.00       | 265.9                             | 8          | 183.5                                    | 8  | 189.1                            | 6   | 183.6         | 7             | -3.08%              |
|                           |                            |                                   | 15         |   | 0.00       |                                  | 0.00       |                                   | 11.        |  | 5. |                                  |     |               | 5.            |                     |
| 39                        | core                       | 0.0510                            | 0.00       | 0.0290                                    | 0.00       | 0.2031                           | 0.00       | 239.9                             | 4          | 184.1                                    | 6  | 187.8                            | 9.5 | 184.2         | 6             | -1.99%              |
|                           |                            |                                   | 12         |   | 0.00       |                                  | 0.01       |                                   |            |  |    |                                  |     |               |               |                     |
| Std02123                  |                            | 0.0514                            | 0.00       | 0.0466                                    | 0.00       | 0.3309                           | 0.01       | 257.0                             | 7          | 293.5                                    | 5  | 290.2                            | 3   | 293.4         | 3             | 1.10%               |

1032  
1033

1034  
1035

| Samp<br>le:<br>Zirco<br>n | FI09C<br>04<br>Positi<br>on | $^{207}\text{Pb}/^{206}\text{Pb}$ |            | Ratio<br>$^{206}\text{Pb}/^{238}\text{U}$ |            | $^{207}\text{Pb}/^{235}\text{U}$ |            | $^{207}\text{Pb}/^{206}\text{Pb}$ |            | Ages<br>$^{206}\text{Pb}/^{238}\text{U}$ |            | $^{207}\text{Pb}/^{235}\text{U}$ |            | U-Pb<br>Concor<br>dia |            | % of<br>discor<br>dance |
|---------------------------|-----------------------------|-----------------------------------|------------|---|------------|----------------------------------|------------|-----------------------------------|------------|--|------------|----------------------------------|------------|-----------------------|------------|-------------------------|
|                           |                             | 1 $\sigma$                        | 2 $\sigma$ | 1 $\sigma$                                | 2 $\sigma$ | 1 $\sigma$                       | 2 $\sigma$ | 1 $\sigma$                        | 2 $\sigma$ | 1 $\sigma$                               | 2 $\sigma$ | 1 $\sigma$                       | 2 $\sigma$ | 1 $\sigma$            | 2 $\sigma$ |                         |
| 26                        | core                        | 0.0588                            | 0.00       | 0.0297                                    | 0.00       | 0.2412                           | 0.00       | 557.8                             | 35.        | 188.9                                    | 4          | 219.4                            | 14.        |                       |            | -16.12%                 |
| 26                        | rim                         | 0.0546                            | 0.00       | 0.0298                                    | 0.00       | 0.2243                           | 0.00       | 394.6                             | 15.        | 189.3                                    | 6          | 205.4                            | 8.8        |                       |            | -8.53%                  |
| 27                        | core                        | 0.0499                            | 0.00       | 0.0287                                    | 0.00       | 0.1975                           | 0.00       | 192.2                             | 12.        | 182.2                                    | 0          | 183.0                            | 11.        | 182.2                 | 4.         | -0.44%                  |
| 28                        | core                        | 0.0513                            | 0.00       | 0.0288                                    | 0.00       | 0.2039                           | 0.00       | 255.7                             | 16.        | 183.2                                    | 0          | 188.4                            | 12.        | 183.2                 | 9          | -2.87%                  |
| 29                        | core                        | 0.0496                            | 0.00       | 0.0305                                    | 0.00       | 0.2088                           | 0.00       | 174.9                             | 14.        | 193.7                                    | 6          | 192.5                            | 15.        | 193.7                 | 5          | 0.62%                   |
| 30                        | core                        | 0.0494                            | 0.00       | 0.0308                                    | 0.00       | 0.2099                           | 0.00       | 165.9                             | 10.        | 195.7                                    | 0          | 193.5                            | 16.        | 195.6                 | 9          | 1.13%                   |
| 31                        | core                        | 0.0482                            | 0.00       | 0.0292                                    | 0.00       | 0.1949                           | 0.00       | 110.1                             | 14.        | 185.4                                    | 9          | 180.8                            | 12.        | 185.3                 | 8          | 2.47%                   |
| 32                        | core                        | 0.0510                            | 0.00       | 0.0291                                    | 0.00       | 0.2042                           | 0.00       | 239.5                             | 14.        | 184.7                                    | 9          | 188.6                            | 12.        | 184.7                 | 8          | -2.15%                  |
| 32                        | rim                         | 0.0493                            | 0.00       | 0.0286                                    | 0.00       | 0.1943                           | 0.00       | 162.6                             | 32.        | 181.6                                    | 5          | 180.3                            | 14.        | 181.5                 | 4          | 0.72%                   |
| 33                        | core                        | 0.0584                            | 0.00       | 0.0328                                    | 0.00       | 0.2645                           | 0.00       | 544.8                             | 10.        | 208.3                                    | 7          | 238.3                            | 4          |                       | 4.         | -14.41%                 |
| 34                        | core                        | 0.0509                            | 0.00       | 0.0298                                    | 0.00       | 0.2093                           | 0.00       | 235.4                             | 27.        | 189.5                                    | 4          | 193.0                            | 11.        | 189.6                 | 7          | -1.85%                  |
| 35                        | core                        | 0.0586                            | 0.00       | 0.0310                                    | 0.00       | 0.2507                           | 0.00       | 553.4                             | 13.        | 196.9                                    | 1          | 227.2                            | 7          |                       |            | -15.39%                 |
| 36                        | core                        | 0.0521                            | 0.00       | 0.0288                                    | 0.00       | 0.2070                           | 0.00       | 287.6                             | 17.        | 183.3                                    | 5          | 191.0                            | 13.        |                       | 5.         | -4.22%                  |
| 37                        | core                        | 0.0513                            | 0.00       | 0.0293                                    | 0.00       | 0.2072                           | 0.00       | 252.1                             | 23.        | 186.0                                    | 2          | 191.2                            | 10.        | 186.1                 | 2          | -2.79%                  |
| 38                        | core                        | 0.0580                            | 0.00       | 0.0308                                    | 0.00       | 0.2461                           | 0.00       | 528.6                             | 36.        | 195.4                                    | 8          | 223.4                            | 11.        |                       |            | -14.33%                 |
| 39                        | core                        | 0.0672                            | 0.00       | 0.0306                                    | 0.00       | 0.2832                           | 0.00       | 842.7                             | 17.        | 194.2                                    | 8          | 253.2                            | 16.        |                       | 5.         | -30.40%                 |
| 40                        | core                        | 0.0501                            | 0.00       | 0.0290                                    | 0.00       | 0.2008                           | 0.00       | 201.5                             | 13.        | 184.2                                    | 7          | 185.8                            | 14.        | 184.2                 | 6          | -0.88%                  |
| 41                        | core                        | 0.0495                            | 0.00       | 0.0286                                    | 0.00       | 0.1957                           | 0.00       | 170.6                             | 17.        | 181.7                                    | 4          | 181.5                            | 14.        | 181.7                 | 4          | 0.08%                   |
| 42                        | core                        | 0.0509                            | 0.00       | 0.0304                                    | 0.00       | 0.2135                           | 0.00       | 234.9                             | 25.        | 193.2                                    | 5          | 196.5                            | 14.        | 193.2                 | 4          | -1.70%                  |
| 43                        | core                        | 0.0592                            | 0.00       | 0.0283                                    | 0.00       | 0.2313                           | 0.00       | 573.7                             | 10.        | 180.2                                    | 5          | 211.3                            | 10.        |                       | 4.         | -17.27%                 |
| 44                        | core                        | 0.0506                            | 0.00       | 0.0289                                    | 0.00       | 0.2011                           | 0.00       | 220.4                             | 13.        | 183.3                                    | 6          | 186.0                            | 10.        | 183.4                 | 5          | -1.45%                  |
| 46                        | core                        | 0.0508                            | 0.00       | 0.0281                                    | 0.00       | 0.1969                           | 0.00       | 232.7                             | 27.        | 178.3                                    | 8          | 182.5                            | 10.        | 178.4                 | 7          | -2.32%                  |
| 47                        | core                        | 0.0602                            | 0.00       | 0.0302                                    | 0.00       | 0.2508                           | 0.00       | 609.7                             | 5.         | 191.9                                    | 9          | 227.2                            | 11.        |                       | 5.         | -18.38%                 |
| 48                        | core                        | 0.0494                            | 0.00       | 0.0301                                    | 0.00       | 0.2048                           | 0.00       | 164.5                             | 13.        | 191.2                                    | 2          | 189.2                            | 11.        | 191.1                 | 1          | 1.04%                   |
| 50                        | core                        | 0.0508                            | 0.00       | 0.0299                                    | 0.00       | 0.2089                           | 0.00       | 230.4                             | 19.        | 189.8                                    | 0          | 192.6                            | 17.        | 189.8                 | 9          | -1.50%                  |
| 51                        | core                        | 0.0502                            | 0.00       | 0.0293                                    | 0.00       | 0.2045                           | 0.00       | 202.4                             | 11.        | 186.4                                    | 1          | 188.9                            | 16.        | 186.4                 | 0          | -1.34%                  |
| 52                        | core                        | 0.0509                            | 0.00       | 0.0291                                    | 0.00       | 0.2042                           | 0.00       | 235.4                             | 15.        | 185.0                                    | 8          | 188.7                            | 16.        | 185.1                 | 7          | -1.96%                  |
| 53                        | core                        | 0.0499                            | 0.00       | 0.0313                                    | 0.00       | 0.2150                           | 0.00       | 189.4                             | 20.        | 198.8                                    | 7          | 197.7                            | 16.        | 198.8                 | 6          | 0.54%                   |
| 54                        | core                        | 0.0510                            | 0.00       | 0.0293                                    | 0.00       | 0.2056                           | 0.00       | 240.4                             | 27.        | 185.9                                    | 9          | 189.9                            | 25.        | 185.9                 | 8          | -2.15%                  |
| Std02123                  |                             | 0.05295                           | 0.00       | 0.0471                                    | 0.00       | 0.3443                           | 0.01       | 326.7                             | 8.         | 297.1                                    | 9          | 300.5                            | 25.        | 297.2                 | 8.         | -1.10%                  |

Table 1: continue.

1036  
1037  
1038

1039  
1040

| Sample: FI09C34 |          | Ratio                             |           |                                  |           |                                  |           | Ages                              |           |                                  |           |                                  |           | U-P       |
|-----------------|----------|-----------------------------------|-----------|----------------------------------|-----------|----------------------------------|-----------|-----------------------------------|-----------|----------------------------------|-----------|----------------------------------|-----------|-----------|
| Zircon          | Position | $^{207}\text{Pb}/^{206}\text{Pb}$ | $1\sigma$ | $^{206}\text{Pb}/^{238}\text{U}$ | $1\sigma$ | $^{207}\text{Pb}/^{235}\text{U}$ | $1\sigma$ | $^{207}\text{Pb}/^{206}\text{Pb}$ | $2\sigma$ | $^{206}\text{Pb}/^{238}\text{U}$ | $2\sigma$ | $^{207}\text{Pb}/^{235}\text{U}$ | $2\sigma$ | Concordia |
| 1               | core     | 0.0494                            | 0.0022    | 0.0290                           | 0.0005    | 0.1977                           | 0.0087    | 166.9                             | 15.2      | 184.5                            | 6.5       | 183.2                            | 16.2      | 184.      |
| 2               | core     | 0.0517                            | 0.0015    | 0.0293                           | 0.0005    | 0.2084                           | 0.0057    | 270.8                             | 15.5      | 186.0                            | 6.0       | 192.2                            | 10.6      | 186.      |
| 3               | core     | 0.0488                            | 0.0023    | 0.0304                           | 0.0005    | 0.2044                           | 0.0093    | 138.2                             | 13.1      | 192.9                            | 6.7       | 188.8                            | 17.2      | 192.      |
| 4               | core     | 0.0492                            | 0.0021    | 0.0292                           | 0.0005    | 0.1987                           | 0.0080    | 157.4                             | 13.2      | 185.6                            | 6.3       | 184.0                            | 14.9      | 185.      |
| 5               | core     | 0.0516                            | 0.0017    | 0.0291                           | 0.0005    | 0.2066                           | 0.0065    | 266.4                             | 17.3      | 184.8                            | 6.2       | 190.7                            | 12.0      | 184.      |
| 6               | core     | 0.0599                            | 0.0017    | 0.0270                           | 0.0005    | 0.2230                           | 0.0062    |                                   |           |                                  |           |                                  |           |           |
| 6               | rim      | 0.0564                            | 0.0014    | 0.0282                           | 0.0004    | 0.2185                           | 0.0052    | 466.6                             | 23.1      | 179.0                            | 5.6       | 200.7                            | 9.5       |           |
| 7               | core     | 3.8182                            | 3.0059    | 0.0285                           | 0.0228    | 15.0262                          | 2.7782    |                                   |           |                                  |           |                                  |           |           |
| 8               | core     | 0.0569                            | 0.0019    | 0.0310                           | 0.0005    | 0.2424                           | 0.0078    | 486.5                             | 32.7      | 196.7                            | 6.5       | 220.4                            | 14.2      |           |
| 10              | core     | 0.0504                            | 0.0012    | 0.0294                           | 0.0004    | 0.2042                           | 0.0046    | 213.0                             | 10.0      | 186.7                            | 5.6       | 188.7                            | 8.4       | 186.      |
| 10              | rim      | 0.0513                            | 0.0030    | 0.0295                           | 0.0006    | 0.2080                           | 0.0120    | 252.1                             | 30.0      | 187.5                            | 7.6       | 191.9                            | 22.1      | 187.      |
| 11              | core     | 0.0506                            | 0.0011    | 0.0296                           | 0.0005    | 0.2070                           | 0.0044    | 224.5                             | 10.1      | 188.3                            | 5.8       | 191.0                            | 8.1       | 188.      |
| Std02123        |          | 0.0530                            | 0.0021    | 0.0464                           | 0.0008    | 0.3388                           | 0.0128    | 329.2                             | 25.9      | 292.1                            | 9.9       | 296.3                            | 22.4      | 292.      |

1041  
1042

Table 1: continue.

1043  
1044Table 2: summary of MC-ICP-MS *in-situ* Hf isotopic compositions of zircon from FPP.

| sample  | zircon | position | Age (Ma) | $^{176}\text{Yb}/^{177}\text{Hf}$ | $2\sigma$ | $^{176}\text{Lu}/^{177}\text{Hf}$ | $2\sigma$ | $^{176}\text{Hf}/^{177}\text{Hf}$ | $2\sigma$ | $e_{\text{Hf}}(0)$ | $e_{\text{Hf}}(t)$ | $2\sigma$ | $T_{\text{DM}}$ | $T_{\text{DM}}^{\text{C}}$ | $f_{\text{Lu/Hf}}$ |
|---------|--------|----------|----------|-----------------------------------|-----------|-----------------------------------|-----------|-----------------------------------|-----------|--------------------|--------------------|-----------|-----------------|----------------------------|--------------------|
| MR01C R | 9      | core     | 188      | 0.001629                          | 0.000039  | 0.000052                          | 0.000001  | 0.282580                          | 0.000015  | -6.77              | 2.65               | 0.5       | 139             | 139                        | -                  |
| MR01C R | 10     | core     | 188      | 0.000730                          | 0.000003  | 0.000022                          | 0.000000  | 0.282582                          | 0.000012  | -6.73              | 2.60               | 0.4       | 927             | 925                        | 1.00               |
| MR01C R | 12     | rim      | 188      | 0.000479                          | 0.000008  | 0.000015                          | 0.000000  | 0.282577                          | 0.000012  | -6.89              | 2.77               | 0.4       | 140             | 140                        | -                  |
| MR01C R | 14     | core     | 188      | 0.000533                          | 0.000025  | 0.000017                          | 0.000000  | 0.282584                          | 0.000012  | -6.64              | 2.51               | 0.4       | 921             | 921                        | 1.00               |
| MR01C R | 16     | core     | 188      | 0.000603                          | 0.000010  | 0.000017                          | 0.000000  | 0.282596                          | 0.000013  | -6.24              | 2.11               | 0.4       | 136             | 136                        | -                  |
| MR01C R | 17     | core     | 188      | 0.000620                          | 0.000019  | 0.000017                          | 0.000000  | 0.282575                          | 0.000011  | -6.96              | 2.83               | 0.4       | 933             | 933                        | 1.00               |
| MR01C R | 20     | core     | 188      | 0.000661                          | 0.000007  | 0.000019                          | 0.000000  | 0.282610                          | 0.000013  | -5.73              | 1.60               | 0.4       | 132             | 132                        | -                  |
| MR01C R | 21     | core     | 188      | 0.000742                          | 0.000012  | 0.000024                          | 0.000000  | 0.282600                          | 0.000011  | -6.09              | 1.97               | 0.3       | 135             | 135                        | -                  |
| MR01C R | 23     | core     | 188      | 0.000550                          | 0.000025  | 0.000017                          | 0.000000  | 0.282553                          | 0.000011  | -7.74              | 3.61               | 0.4       | 145             | 145                        | -                  |
| MR01C R | 24     | core     | 188      | 0.000573                          | 0.000004  | 0.000017                          | 0.000000  | 0.282585                          | 0.000013  | -6.61              | 2.48               | 0.4       | 920             | 920                        | 1.00               |
| MR01C R | 25     | rim      | 188      | 0.000420                          | 0.000006  | 0.000013                          | 0.000000  | 0.282550                          | 0.000012  | -7.85              | 3.73               | 0.4       | 146             | 146                        | -                  |
| MR01C R | 26     | core     | 188      | 0.000534                          | 0.000006  | 0.000016                          | 0.000000  | 0.282552                          | 0.000013  | -7.79              | 3.66               | 0.4       | 145             | 145                        | -                  |
| MR01C R | 27     | core     | 188      | 0.000836                          | 0.000026  | 0.000025                          | 0.000000  | 0.282595                          | 0.000012  | -6.25              | 2.12               | 0.4       | 136             | 136                        | -                  |
| MR01C R | 28     | core     | 188      | 0.000461                          | 0.000007  | 0.000013                          | 0.000000  | 0.282601                          | 0.000013  | -6.05              | 1.92               | 0.4       | 134             | 134                        | -                  |
| MR01C R | 30     | core     | 188      | 0.000492                          | 0.000005  | 0.000014                          | 0.000000  | 0.282599                          | 0.000013  | -6.11              | 1.98               | 0.4       | 135             | 135                        | -                  |
| MR01C R | 30     | rim      | 188      | 0.000990                          | 0.000022  | 0.000033                          | 0.000000  | 0.282556                          | 0.000020  | -7.63              | 3.51               | 0.7       | 144             | 144                        | -                  |
| MR01C R | 33     | core     | 188      | 0.000382                          | 0.000015  | 0.000012                          | 0.000000  | 0.282564                          | 0.000013  | -7.34              | 3.22               | 0.4       | 143             | 143                        | -                  |
| MR01C R | 34     | core     | 188      | 0.000404                          | 0.000011  | 0.000012                          | 0.000000  | 0.282570                          | 0.000014  | -7.15              | 3.03               | 0.4       | 141             | 141                        | -                  |
| MR01C R | 35     | core     | 188      | 0.000783                          | 0.000007  | 0.000024                          | 0.000000  | 0.282601                          | 0.000015  | -6.05              | 1.92               | 0.5       | 134             | 134                        | -                  |
| MR01C R | 38     | core     | 188      | 0.000403                          | 0.000020  | 0.000013                          | 0.000000  | 0.282572                          | 0.000012  | -7.06              | 2.93               | 0.4       | 141             | 141                        | -                  |
| MR01C R | 39     | core     | 188      | 0.000409                          | 0.000004  | 0.000012                          | 0.000000  | 0.282570                          | 0.000015  | -7.16              | 3.03               | 0.5       | 141             | 141                        | -                  |
| FI09C04 | 26     | core     | 188      | 0.000531                          | 0.000005  | 0.000021                          | 0.000000  | 0.282527                          | 0.000019  | -8.68              | 4.55               | 0.6       | 100             | 151                        | -                  |
| FI09C04 | 26     | rim      | 188      | 0.000872                          | 0.000019  | 0.000033                          | 0.000000  | 0.282566                          | 0.000016  | -7.27              | 3.15               | 0.5       | 142             | 142                        | -                  |
| FI09C04 | 27     | core     | 188      | 0.000569                          | 0.000005  | 0.000022                          | 0.000000  | 0.282550                          | 0.000016  | -7.85              | 3.72               | 0.5       | 946             | 946                        | 1.00               |
| FI09C04 | 28     | core     | 188      | 0.000576                          | 0.000024  | 0.000024                          | 0.000000  | 0.282582                          | 0.000016  | -6.74              | 2.61               | 0.5       | 146             | 146                        | -                  |
| FI09C04 | 29     | core     | 188      | 0.000577                          | 0.000005  | 0.000022                          | 0.000000  | 0.282579                          | 0.000016  | -6.74              | 2.61               | 0.5       | 925             | 925                        | 1.00               |
| FI09C04 | 30     | core     | 188      | 0.000442                          | 0.000007  | 0.000017                          | 0.000000  | 0.282534                          | 0.000016  | -8.41              | 4.28               | 0.5       | 139             | 139                        | -                  |
| FI09C04 | 31     | core     | 188      | 0.001212                          | 0.000003  | 0.000047                          | 0.000000  | 0.282523                          | 0.000019  | -8.81              | 4.69               | 0.6       | 100             | 152                        | -                  |
| FI09C04 | 32     | core     | 188      | 0.000572                          | 0.000009  | 0.000022                          | 0.000000  | 0.282554                          | 0.000010  | -7.71              | 3.58               | 0.7       | 145             | 145                        | -                  |
| FI09C04 | 33     | core     | 188      | 0.000638                          | 0.000009  | 0.000025                          | 0.000000  | 0.282546                          | 0.000018  | -7.99              | 3.86               | 0.6       | 963             | 963                        | 1.00               |
| FI09C04 | 34     | core     | 188      | 0.000613                          | 0.000007  | 0.000024                          | 0.000000  | 0.282528                          | 0.000017  | -8.63              | 4.51               | 0.5       | 147             | 147                        | -                  |
| FI09C04 | 35     | core     | 188      | 0.000626                          | 0.000008  | 0.000025                          | 0.000000  | 0.282528                          | 0.000011  | -8.64              | 4.52               | 0.7       | 151             | 151                        | -                  |
| FI09C04 | 36     | core     | 188      | 0.000754                          | 0.000009  | 0.000028                          | 0.000000  | 0.282489                          | 0.000019  | 10.00              | 5.88               | 0.6       | 105             | 159                        | -                  |

|         |    |      |     |          |          |          |          |          |          |       |      |     |     |     |   |      |
|---------|----|------|-----|----------|----------|----------|----------|----------|----------|-------|------|-----|-----|-----|---|------|
| FI09C04 | 37 | core | 188 | 0.000605 | 0.000011 | 0.000025 | 0.000000 | 0.282582 | 0.000021 | -6.71 | 2.59 | 0.7 | 139 | -   |   |      |
| FI09C04 | 38 | core | 188 | 0.000544 | 0.000011 | 0.000021 | 0.000000 | 0.282486 | 0.000018 | -     | -    | 0.6 | 105 | 160 |   |      |
| FI09C04 | 39 | core | 188 | 0.000619 | 0.000011 | 0.000026 | 0.000000 | 0.282524 | 0.000021 | -8.76 | 4.64 | 0.7 | 100 | 152 |   |      |
|         |    |      |     |          |          |          |          |          |          |       |      |     | 4   | 3   | 0 | 1.00 |

1045

| sample  | zirco<br>n | position | Age<br>(Ma) | $^{176}\text{Yb}/^{177}\text{H}$<br>f | $2\sigma$ | $^{176}\text{Lu}/^{177}\text{H}$<br>f | $2\sigma$ | $^{176}\text{Hf}/^{177}\text{H}$<br>f | $2\sigma$ | $e_{\text{Hf}}(0)$ | $e_{\text{Hf}}(t)$ | $2\sigma$ | $T_{\text{DM}}$ | $T_{\text{DM}}^{\text{C}}$ | $f_{\text{Lu/Hf}}$ |
|---------|------------|----------|-------------|---------------------------------------|-----------|---------------------------------------|-----------|---------------------------------------|-----------|--------------------|--------------------|-----------|-----------------|----------------------------|--------------------|
| FI09C04 | 40         | core     | 188         | 0.000497                              | 0.000018  | 0.000020                              | 0.000001  | 0.282522                              | 0.000023  | -8.84              | 4.71               | 0.8       | 100             | 152                        | -                  |
| FI09C04 | 41         | core     | 188         | 0.000628                              | 0.000008  | 0.000024                              | 0.000000  | 0.282522                              | 0.000022  | -8.84              | 4.72               | 0.7       | 100             | 152                        | -                  |
| FI09C04 | 42         | core     | 188         | 0.000493                              | 0.000006  | 0.000020                              | 0.000000  | 0.282553                              | 0.000016  | -7.73              | 3.61               | 0.5       |                 | 145                        | -                  |
| FI09C04 | 44         | core     | 188         | 0.000690                              | 0.000012  | 0.000025                              | 0.000000  | 0.282536                              | 0.000017  | -8.36              | 4.23               | 0.5       |                 | 149                        | -                  |
| FI09C04 | 46         | core     | 188         | 0.000976                              | 0.000018  | 0.000037                              | 0.000000  | 0.282576                              | 0.000018  | -6.94              | 2.81               | 0.6       | 101             | 153                        | -                  |
| FI09C04 | 48         | core     | 188         | 0.000558                              | 0.000009  | 0.000022                              | 0.000000  | 0.282518                              | 0.000018  | -8.97              | 4.85               | 0.6       | 101             | 153                        | -                  |
| FI09C04 | 50         | core     | 188         | 0.000510                              | 0.000018  | 0.000022                              | 0.000001  | 0.282578                              | 0.000017  | -6.86              | 2.74               | 0.6       | 101             | 153                        | -                  |
| FI09C04 | 51         | core     | 188         | 0.000901                              | 0.000005  | 0.000035                              | 0.000000  | 0.282519                              | 0.000017  | -8.96              | 4.84               | 0.6       | 101             | 153                        | -                  |
| FI09C04 | 52         | core     | 188         | 0.001005                              | 0.000005  | 0.000041                              | 0.000001  | 0.282544                              | 0.000019  | -8.05              | 3.93               | 0.6       | 101             | 153                        | -                  |
| FI09C04 | 53         | core     | 188         | 0.000646                              | 0.000010  | 0.000026                              | 0.000000  | 0.282550                              | 0.000018  | -7.84              | 3.72               | 0.6       | 101             | 153                        | -                  |
|         |            |          |             |                                       |           |                                       |           |                                       |           |                    |                    |           | 968             | 2                          | 1.00               |
| FI09C34 | 1          | core     | 188         | 0.000808                              | 0.000017  | 0.000031                              | 0.000000  | 0.282503                              | 0.000020  | -9.52              | 5.40               | 0.6       | 103             | 156                        | -                  |
| FI09C34 | 2          | core     | 188         | 0.000783                              | 0.000020  | 0.000032                              | 0.000001  | 0.282532                              | 0.000019  | -8.50              | 4.38               | 0.6       | 103             | 156                        | -                  |
| FI09C34 | 3          | core     | 188         | 0.000886                              | 0.000009  | 0.000038                              | 0.000000  | 0.282530                              | 0.000022  | -8.55              | 4.43               | 0.7       | 103             | 156                        | -                  |
| FI09C34 | 4          | core     | 188         | 0.000575                              | 0.000014  | 0.000023                              | 0.000000  | 0.282529                              | 0.000018  | -8.58              | 4.45               | 0.6       | 103             | 156                        | -                  |
| FI09C34 | 5          | core     | 188         | 0.000646                              | 0.000012  | 0.000028                              | 0.000000  | 0.282492                              | 0.000018  | -9.90              | 5.78               | 0.6       | 104             | 159                        | -                  |
| FI09C34 | 6          | rim      | 188         | 0.000925                              | 0.000006  | 0.000039                              | 0.000001  | 0.282551                              | 0.000032  | -7.80              | 3.68               | 1.1       | 104             | 159                        | -                  |
| FI09C34 | 8          | core     | 188         | 0.000498                              | 0.000004  | 0.000019                              | 0.000000  | 0.282577                              | 0.000018  | -6.90              | 2.78               | 0.6       | 104             | 159                        | -                  |
| FI09C34 | 10         | core     | 188         | 0.000427                              | 0.000008  | 0.000018                              | 0.000000  | 0.282529                              | 0.000020  | -8.59              | 4.46               | 0.7       | 104             | 159                        | -                  |
| FI09C34 | 10         | rim      | 188         | 0.000651                              | 0.000007  | 0.000029                              | 0.000000  | 0.282587                              | 0.000019  | -6.55              | 2.43               | 0.6       | 104             | 159                        | -                  |
| FI09C34 | 11         | core     | 188         | 0.000881                              | 0.000017  | 0.000039                              | 0.000000  | 0.282533                              | 0.000017  | -8.46              | 4.34               | 0.5       | 104             | 159                        | -                  |
|         |            |          |             |                                       |           |                                       |           |                                       |           |                    |                    |           | 992             | 2                          | 1.00               |

Table 2: continue.

1046

1047

1048  
1049  
1050  
1051  
1052

Table 3: Isotopic oxygen composition ( $\delta^{18}\text{O}$  vs. SMOW‰) of mineral separates from the FPP chromitites here studied. Numbers between parenthesis represent the number of replicates of the measurements on different aliquots of the same sample.

| Sample  | Phase   | $\delta^{18}\text{O}$ avg. | Std. Dev. |
|---------|---------|----------------------------|-----------|
| MR01CR  | Zrc (1) | 6.80                       | 0.05      |
|         | Opx (2) | 5.36                       |           |
| FI09C04 | Opx (2) | 6.86                       | 0.05      |
|         | Cpx (3) | 6.73                       | 0.06      |
| FI09C34 | Opx (2) | 6.76                       | 0.06      |
|         | Cpx (2) | 6.53                       | 0.06      |

1053

ACCEPTED MANUSCRIPT

1054 **Highlights:**

- 1055 zircon-bearing mantle chromitites formed along with the Finero phlogopite harzbugites  
1056 the Finero Phlogopite Peridotite was firstly metasomatised in Early Permian or before  
1057 younger ages record thermal perturbations related to tectono-magmatic events  
1058 the exhumation of Finero Phlogopite Peridotite occurred in Early Jurassic  
1059 the IVZ exhumation was accompanied by a thermal perturbation at ~187 Ma

ACCEPTED MANUSCRIPT